Well-designed ZnV_2O_6/g-C_3N_4 2D/2D nanosheets heterojunction with faster charges separation via pCN as mediator towards enhanced photocatalytic reduction of CO_2 to fuels

Abdullah Bafaqeer, Muhammad Tahir*, Nor Aishah Saidina Amin

Chemical Reaction Engineering Group (GREG), School of Chemical and Energy Engineering, Universiti Teknologi Malaysia, 81310, UTM, Johor Bahru, Johor, Malaysia

ABSTRACT

Fabrication of well-designed 2D/2D heterojunction composite with effective interfacial contact by incorporating zinc vanadium oxide (ZnV_2O_6) and protonated g-C_3N_4 (pCN) for enhanced photocatalytic CO_2 reduction has been investigated. The 2D/2D ZnV_2O_6/pCN samples, synthesized by a one-pot solvothermal method, were analysed using XRD, SEM, EDX-mapping, TEM, N_2 sorption, XPS, UV–vis, RAMAN and PL characterization techniques. It was observed that surface charge modification through protonation of graphitic carbon nitride serves as a mediator and trapped photo-excited electrons. The performance of composite catalysts was investigated in a liquid and gas phase photocatalytic systems under UV and visible light irradiations. Using slurry system, CH_3OH production rate enhanced up to 3742 μmol g-cat^{-1} over ZnV_2O_6/pCN, 1.15 and 5 times higher than the pure ZnV_2O_6 (3254 μmol g-cat^{-1}) and pCN (753 μmol g-cat^{-1}) samples, respectively. Instead, the CO evolution rate as a main product over ZnV_2O_6/pCN nanosheets of 3237 μmol g-cat^{-1} was obtained using gas phase system. This enhanced activity can be mainly ascribed to the addition of pCN with ZnV_2O_6 in a controlled ratio as well as synergistic effect of ZnV_2O_6/pCN nanosheet heterojunctions. Besides, hierarchical structure, higher interfacial interaction, abundant 2D coupling interfaces and efficient separation of charges could efficiently promote both the photo-activity and products selectivity. The obtained ZnV_2O_6/pCN 2D/2D nanosheets heterojunction with a mediator exhibited excellent photocatalytic stability, which prevailed even after 32 h of operation time for continuous CH_3OH production. The possible reaction mechanism anticipated to understand the movement of electrons and holes for CO_2 reduction over the ZnV_2O_6/pCN photocatalyst.

1. Introduction

Photocatalytic reduction of CO_2 with water into renewable hydrocarbon solar fuels is considered as a promising strategy to simultaneously address the global energy and environmental issues. Although, there are many photocatalysts reported for reduction of CO_2, the improvement of activity and selectivity is still in great need of [1–5]. Since 1979, Inoue et al. [6] first reported photocatalytic CO_2 reduction over semiconductor materials, many research groups have studied photocatalytic mechanism and efficiency of CO_2 conversion into renewable fuels such as CH_3OH, HCOOH, HCHO, CO and CH_4 over several semiconductors, including TiO_2 [7–10], Ta_2O_5 [11], ZnO [12,13] and CdS [14]. However, these semiconductors display unsatisfactory photo-activity because of rapid charges recombination and limited visible-light harvesting. Therefore, it is of great importance to design and develop efficient and selective photo-catalysts for visible light driven CO_2 reduction applications.

Recently, graphitic carbon nitride (g-C_3N_4) has gained massive recognition because of its abundance, easy preparation from cheap and available precursors, and chemical stability. During the last years, g-C_3N_4 as a photo-catalyst has been widely investigated in photo-oxidation reactions like photo-production of hydrogen, photo-degradation of dyes, and oxidation of alcohols [15]. Although, g-C_3N_4 is a visible-light responsive, but it is limited by small specific area, high recombination rate and low photocatalytic activity [16]. Several efforts have been made to promote the performance of g-C_3N_4 such as metal [17] and non-metal doping [18] and formation of g-C_3N_4 based composites [19]. Protonation is considered as an effective and facile method to enrich g-C_3N_4 with specific properties such as ferromagnetism and solubility since the early report by Wang et al. in 2008 [20–22]. Recently, modification process was proposed to affect surface charge properties, which could be utilized to construct assembled catalysts [23–25].

However, this treatment provides a new strategy of designing light harvesting substrates with promoted charge separation efficiency, which can be used to enhanced activity for visible light driven CO_2 reduction to methanol. Modification by formation of g-C_3N_4 based composites and heterostructures have displayed great progress because it fosters separation of charges, reduces the band gap of co-dopants and allows for a synergistic interaction [26–28]. Thus, many research efforts have been made to develop efficient photocatalysts for the reduction of CO_2 to fuels such as g-C_3N_4/WO_3 [29], ZnO/g-C_3N_4 [30], g-C_3N_4/SnS_2 [31], MnO_2/g-C_3N_4 [32], g-C_3N_4/ZnO [33] and g-C_3N_4/NiAl [34]. Therefore, it is appropriate to develop protonated g-C_3N_4 based semiconductors for enhanced photocatalytic CO_2 reduction applications under solar energy.

Recently, ternary nanostructures have received much attention and demonstrated remarkable performances in photocatalytic reduction of CO_2 and other device applications [35–38]. Furthermore, the construction of a semiconductor heterojunction has garnered enormous attention due to its perfect effectiveness in improving the photocatalytic activity [39]. In this perspective, the $ZnIn_2S_4$/TiO_2 composite has shown significantly enhanced photocatalytic activity compared with the bare semiconductors [40]. Similarly, enhanced photo-activity has been reported over Cu_2ZnSnS_4/ZnO composite catalyst for photocatalytic reduction of CO_2 to CH_4 [41]. Recently, Zn_2GeO_4/Mg-MOF-74 composites with enhanced photocatalytic activity for CO_2 reduction has been reported [42]. However, ternary ZnVO based semiconductors have gained attention recently due to its interesting structural changes at low temperature [43]. Different nanostructures of ZnVO have been reported such as nanosheets, hollow spheres, and glomerulus nano/microspheres for various applications [43–45]. They have displayed good charge-discharge performance in lithium ion batteries and a promising photocatalyst. Besides, hierarchical ZnVO nanosheets are equally interesting due to their layered structures and strong visible absorption [35,46]. Moreover, the construction of g-C_3N_4 based ternary semiconductors such as g-C_3N_4/$BiVO_4$ [47], $LaPO_4$/g-C_3N_4 [48], g-C_3N_4/$NaNbO_3$ [49] and $Bi_{12}GeO_{20}$/g-C_3N_4 [50] has shown significantly enhanced photocatalytic activity. Therefore, it is highly desirable to construct protonated 2D g-C_3N_4 modified 2D ZnV_2O_6 composite heterojunction to enhance photocatalytic CO_2 reduction to fuels under visible light irradiations.

Herein, we have designed and demonstrated a new 2D/2D ZnV_2O_6/protonated g-C_3N_4 (pCN) nanosheets heterojunction through a one-step solvothermal process. The acid pre-treatment with HNO_3 can easily alter the g-C_3N_4 to possess positive polarity and can serve as a mediator for electron trapping. The samples were characterized using techniques which include XRD, SEM, XPS, EDX-mapping, HRTEM, N_2 adsorption-desorption, RAMAN, UV–vis and PL spectroscopy. The performance of the catalysts was tested under UV and visible light irradiations in a slurry and gas phase systems. The obtained 2D/2D ZnV_2O_6/pCN nanosheets displayed enhanced photocatalytic activity for converting CO_2 to CH_3OH, CO, CH_4 and hydrocarbons. The stability of the samples was analysed based on the cyclic runs for continuous methanol production under visible light irradiations. Finally, feasible reaction mechanism has been proposed based on the experimental results.

2. Experimental

2.1. Materials

Zinc acetate (Sigma-Aldrich, 99.99%), melamine (Sigma-Aldrich, 99.0%), N,N-dimethyl formamide (Sigma-Aldrich, 99.8%), NH_3 solution (Merck, 25%), Oxalic acid dehydrated (QReC, 126.07 g/mol), zinc oxide (Sigma-Aldrich) and ammonium metavanadate (Merck, 116.97 g/mol) were used as received. All other reagents used in this work were analytically pure and used without further purification.

2.2. Preparation of ZnO/V_2O_5 composite

The ZnO/V_2O_5 composite was prepared using sol-gel method. Typically, 0.5 g of ammonium metavanadate [NH_4VO_3] was dissolved into 40 mL deionized water and then adjusted the solution pH to 9 using 2 M NH_3 solution. After stirring for 15 min, ZnO (Sigma-Aldrich) was added to above solution and stirred for 1 h. The precipitates collected were washed several times with deionized water. Then, the products were dried in oven under air flow at 80 °C for 12 h. Finally, samples ZnO/V_2O_5 composite were calcined at 550 °C for 3 h to get ZnO/V_2O_5 composite. The V_2O_5 sample was prepared using the same procedures except the addition of ZnO.

2.3. Preparation of hierarchical 2D ZnV_2O_6 nanosheets

The ZnV_2O_6 nanosheets were obtained using a previously reported procedure [35,46]. Typically, 2.052 mmol of ammonium metavanadate [NH_4VO_3] was added into 20 ml of N,N-dimethyl formamide (DMF). After stirring for 10 min, zinc acetate [$Zn(O_2CCH_3)_2$] was added to above solution under continuous stirring to obtain a colloidal solution. Oxalic acid dehydrated [$H_2C_2O_4 \cdot 2H_2O$] with oxalic acid to NH_4VO_3 ratio of 1:3 was added afterwards. After stirring for 30 min, solution was transferred into a 75 ml Teflon lined autoclave, which was maintained at 200 °C for 24 h and then cooled to room temperature naturally to get black colour product. The precipitates collected were washed for several times with absolute ethanol. Finally, the products were dried in air flow oven at 80 °C for 12 h. The as prepared ZnV_2O_6 were calcined at 550 °C for 3 h and efficiency between as prepared and calcined materials was compared. Different ZnV_2O_6 samples were prepared with exposure times of heating for 12 h, 48 h and 72 h using the same procedure.

2.4. Synthesis of proton-functionalized g-C_3N_4 (pCN) photo-catalyst

Bulk g-C_3N_4 was fabricated by thermal treatment of melamine [51]. In a typical process, 4 g of melamine was added in a crucible with a lid to decrease sublimation of melamine. The crucible was put in a muffle furnace and heated to 550 °C for 3 h. After cooled to room temperature, the light-yellow product was collected and ground to get fine powder. Afterwards, 1 g of the as-obtained bulk g-C_3N_4 was added into 0.1 mol/L of HNO_3 aqueous solution and stirred for 4 h at room temperature for its protonation. The mixture was filtered and repeatedly washed with DI water to remove superfluous HNO_3 until the pH of the filtrate water became neutral. Finally, the pCN product was dried at 80 °C for 12 h and grounded into fine powder.

2.5. Synthesis of pCN-modified ZnV_2O_6 (ZnV_2O_6/pCN) nanosheets

In a typical synthesis, 2.052 mmole of ammonium metavanadate [NH_4VO_3] was added into 20 ml of N,N-dimethyl formamide (DMF). After 10 min., Zinc acetate [$Zn(O_2CCH_3)_2$] was added to above solution and suspension was allowed to stir for few minutes to obtain a colloidal solution. Later, oxalic acid dehydrated [$H_2C_2O_4 \cdot 2H_2O$] was added by adjusting ratio of oxalic acid to NH_4VO_3 of 1:3. Afterwards, a certain amount of protonated g-C_3N_4 (pCN) was added into the solution and stirred for 30 min. Finally, the obtained solution was transferred into a 75 mL Teflon lined autoclave, which was maintained at 200 °C for 24 h and then cooled to room temperature. The precipitates were collected, washed for several times with absolute ethanol, and then dried in an oven under 80 °C for 12 h. A series of ZnV_2O_6-pCN nanosheets with different weight addition ratios of pCN to nanosheets (50%, 100%, 150%) were obtained using the same procedure. The mass ratios of the ZnV_2O_6/pCN (50%), ZnV_2O_6/pCN (100%) and ZnV_2O_6/pCN (100%) samples are 1:0.5, 1:1 and 1:1.5, respectively.

2.6. Characterization of materials

The crystalline structure of the catalysts was ascertained by X-ray diffractometer (Rigaku Smart Lab) Cu-Kα radiation (λ = 0.154178 nm) operated at 40 kV and 30 mA. The XRD patterns were obtained with a scanning rate of 0.02° min^{-1} and scanning range of 3–90° of 2θ. Nitrogen-adsorption-desorption isotherms were collected using Micrometrics ASAP 2020 at 77 K, after degassing the samples at 523 K for 4 h under vacuum and using the nitrogen flux. The BET surface area and pore diameter were calculated from the desorption branch of isotherms according to BJH method. The surface morphology and EDX mapping analysis of the samples was examined using field emission scanning electron microscopy (FE-SEM, ZEISS Crossbeam 340). The high-resolution transmission electron microscope (HR-TEM) images of the modified nanoparticles were obtained in a transmission electron microscope (TEM, HITACHI HT7700). The investigation on surface component elemental state was analysed using X-ray photoelectron spectroscopy (XPS, Axis Ultra DLD Shimadzu). The XPS spectra were calibrated with respect to the binding energy of the C 1s signal at 284.60 V as the internal standard. Ultraviolet–vis (UV–vis) diffuse reflectance absorbance spectra were carried out on a Cary 100 Agilent UV–vis spectrophotometer (Model G9821 A) equipped with an integrated sphere in the wavelength range of 200–800 nm. Raman and photoluminescence (PL) spectra of the samples were recorded at room temperature using Raman Spectrometer (Lab RAM HR Evolution, HORIBA), whereas PL was conducted using a laser of 325 nm and RAMAN with a laser of 532 nm as excitation source.

2.7. Photocatalytic activity test

The photocatalytic CO_2 reduction with H_2O in a liquid phase was carried out in a jacketed Pyrex glass slurry photoreactor with a total volume of 150 mL as depicted in Fig. 1(a). Cooling water from a chiller was passed through the jacketed wall of the reactor to control the temperature. A 35 W HID Xe lamp was used as a visible light source with a light intensity of 20 mW cm^{-2} measured using a reference solar cell (91,150 V, Newport) [52]. First, 100 mg powder photo-catalyst was added into 100 ml distilled water containing 0.1 M NaOH solution in a glass reactor under magnetic stirring. Then, compressed CO_2 gas regulated by mass flow controller (MFC) was bubbled through the solution for 30 min to remove any oxygen before starting the experiment. The temperature of the reactor was maintained at 25 °C by circulating cold water from a chiller. The controlled experiments were conducted at 25 °C, 1 atm and feed flow rate of 20 mL/min. The lamp was turned on to start the photoreaction under continuous CO_2 flow rate though the reactor. During the reaction process, the liquid products were taken out after 2 h interval using a syringe. The drawn samples were filtered using Syringe Filter with Nylon Membrane, pore size 0.45 μm and diameter 33 mm in order to remove particles of the catalyst. The concentration of methanol was analyzed by a gas chromatograph (GC-7820 A) equipped with a flame ionization detector (FID) and HP-5 capillary column. The calibration of the GC was conducted using standard solutions of methanol.

Furthermore, gas phase photocatalytic reduction of CO_2 with H_2O was carried out in a stainless steel photoreactor as shown in Fig. 1(b). A 200 W Hg reflector lamp with a light intensity of 150 mW/cm^2 was used as a source of UV-light irradiation. The photoactivity was further investigated using a solar simulator LCS-100 integrated with UV-cut filters with light intensity of 100 mW/cm^2. The lamps were located at the top of the reactor equipped with a quartz window for passing of light irradiations and cooling fans were used to remove lamp heat. Typically, 100 mg powder photo-catalyst was dispersed uniformly at the bottom of the cylindrical stainless-steel chamber. Compressed CO_2 (99.999%) regulated by a mass flow controller (MFC) was bubbled through water saturator to carry moisture. For CO_2 reduction under continuous flow operation, gas was continuously passed through the reactor at a total

gas flow rate of 5 mL/min. The products were analysed using an online gas chromatograph (GC Agilent Technologies 6890 N, USA) equipped with FID and TCD detectors (GC/FID/TCD). The FID detector was connected with a HP-PLOT Q capillary column (Agilent, length 30 m, ID 0.53 mm, film 40 μm) while he TCD detector was connected to UCW982, DC-200, Porapak Q and Mol Sieve 5 A columns. Control experiments were carried out in the dark or without catalyst under the same experimental conditions. The carbon containing products were not detected in the absence of light irradiation or catalysts.

3. Results and discussion

3.1. Characterization of catalysts

Fig. 2(a) shows XRD patterns of as synthesized and calcined ZnV_2O_6 samples. Clearly, the XRD pattern of the ZnV_2O_6 nanosheets (blue curve) shows one pronounced diffraction peak located at around 2θ = 10.0°. Such a diffraction pattern can be attributed to metal alkoxides [53,54]. As expected, the ZnV_2O_6 nanosheets can be converted into highly crystalline material after calcining at 550 °C for 3 h in air atmosphere. All the identified diffraction peaks (red curve) can be assigned to ZnV_2O_6 with an orthorhombic structure (JCPDS Card No. 01-074-1262). Also, weak diffraction peaks of V_2O_5 appeared, which indicated that a small amount of V_2O_5 (JCPDS Card No. 01-072-0433) was generated and the resulting sample was a mixture of ZnV_2O_6 nanosheets and V_2O_5.

Fig. 2(b) displays the XRD patterns of the as-prepared pCN, ZnV_2O_6 and ZnV_2O_6/pCN nanocomposites. Two typical diffraction peaks of g-C_3N_4 [55] were still present in the pCN after acid pre-treatment process, highlighting that the atomic structures of g-C_3N_4 were well-maintained. The strong diffraction peak at 27.3° listed at plane (002) is representative of the interlayer stacked conjugated aromatic system. On the other hand, the weak diffraction peak at 13.11° listed at plane (100) represents the intra-planar structural packing of the aromatic system. Presence of these two typical peaks of pCN confirms its identity. However, two pronounced peaks were found in pCN at 27.3° and 13.11° [56]. Pure ZnV_2O_6 exhibits several peaks at 14.4°, 21.4° and 31.3° (JCPDS Card No. 01-074-1262). For the ZnV_2O_6/pCN composite, the XRD patterns display a combination of the two sets of diffraction data for both ZnV_2O_6 and pCN. Thus, the results indicated the presence of two phases, ZnV_2O_6 and pCN, in the composite sample. With the increase in pCN content, the peaks of ZnV_2O_6/pCN composite were not affected.

The surface area (S_{BET}), BJH surface area (S_{BJH}) and t-Plot micro pore volume of all samples are summarized in Table 1. The BET surface area of 11.57, 5.22, 10.98 and 11.26 m^2/g was obtained for bare ZnV_2O_6, ZnV_2O_6 calcined, pCN and ZnV_2O_6/pCN, respectively. The BET surface area of 11.57 m^2/g for ZnV_2O_6 was higher than the BET surface of ZnV_2O_6 calcined (5.22 m^2/g). This was perhaps because of their different hierarchical structures. On the other hand, BET surface area gradually decreased to 11.26 m^2/g, when 100 wt.% pCN was combined to ZnV_2O_6 nanosheets. This decreased in the BET surface area could be accounted for partial ZnV_2O_6 nanosheets surface coverage by the deposited pCN. However, the BJH surface area somewhat increased with pCN combined, approving higher mesoporosity in pCN-combined ZnV_2O_6 nanocomposites than bare ZnV_2O_6 samples. The t-plot micropores gradually decreased with pCN combined ZnV_2O_6, possibly due to pCN nanosheets distributed over the ZnV_2O_6 layers, having lower pore volumes. Thus, the decreased in pore volume would possibly because of the dispersion of pCN over ZnV_2O_6 nanosheets.

Fig. 3 exhibits FESEM images of the pure pCN, ZnV_2O_6, ZnV_2O_6 calcined and ZnV_2O_6/pCN (100%) nanosheets. As depicted in Fig. 3(a), after acid pre-treatment of pure g-C_3N_4, the exfoliated pCN presented a 2D morphology, a layered, flat, sheet-like structure having hollows and a lamellar structure. It can be seen in Fig. 3(b) that the ZnV_2O_6 sample prepared at 12 h reaction time composed of intermediate products
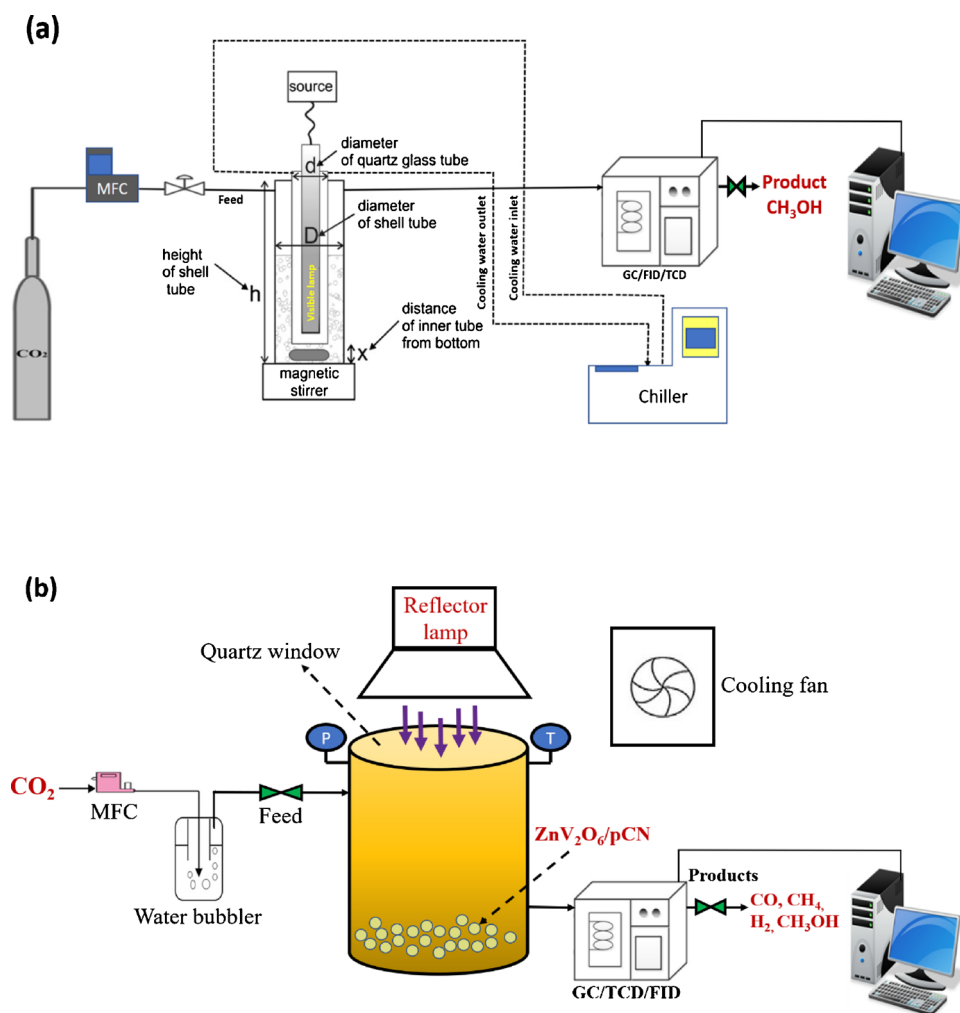
Fig. 1. (a) Schematic of experimental set-up for CO_2 reduction in a slurry photoreactor system under visible light; (b) Experimental set-up for photo-catalytic CO_2 in presence of H_2O in a gas phase photoreactor under UV and Visible light.
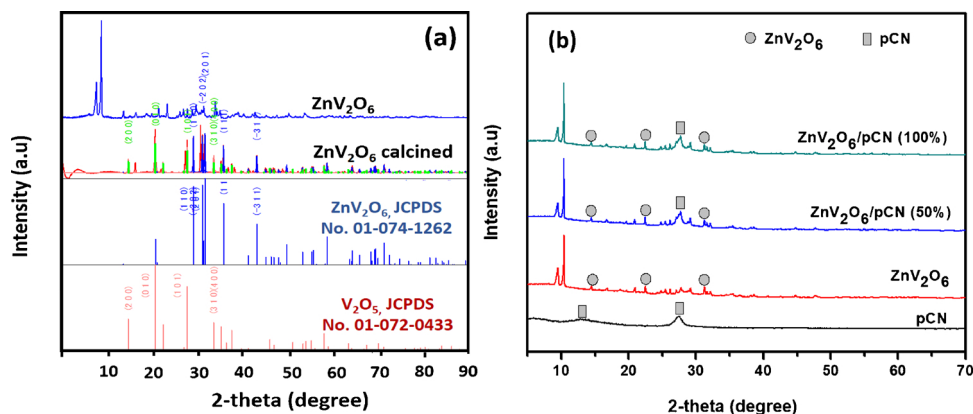

Fig. 2. XRD patterns of (a) ZnV_2O_6 and ZnV_2O_6 calcined and (b) pCN, ZnV_2O_6, ZnV_2O_6/pCN (50%) and ZnV_2O_6/pCN (100%) samples.

which consists of many compact sheets. However, when the reaction time was increased to 24 h, large amounts of sheets were formed as shown in Fig. 3(c). Clearly, pure ZnV_2O_6 has hierarchical microstructure consisting of uniform size nanosheets. Furthermore, when the ZnV_2O_6 nanosheets, prepared after 24 h reaction time, were calcined at 550 °C for 3 h, they were partially disordered with improved surface roughness and reduced in size as shown in Fig. 3(d). This revealed that calcination temperature has an impact on the structure and morphology of ZnV_2O_6 nanosheets. Fig. 3(e and f) shows the micrograph of pCN

sheets with a fold surface, the ZnV_2O_6 substrate is partly covered by the pCN nanosheets which reveals a good interaction between ZnV_2O_6 and pCN nanosheets

Fig. 4 exhibits EDX analysis of pCN combined with ZnV_2O_6 2D/2D nanosheets. Fig. 4 (a) and (b) depicts the presence of pCN over the ZnV_2O_6 nanosheets. It can be observed that pCN are entirely distributed over the surface of ZnV_2O_6 nanosheets. Zinc, vanadium, oxygen, carbon and nitrogen were the elements found by EDX analysis as displayed in Fig. 4(c). The presence of Pt was due platinum used for FESEM analysis.

Table 1
Summary of physiochemical characteristics of photocatalysts.

Sample	BET surface area S_{BET} (m²/g)	BJH surface area S_{BJH} (m²/g)	t-Plot micropore volume (cm³/g)	Band gap (E_{bg})
ZnV_2O_6	11.57	3.80	0.0045	2.02
ZnV_2O_6 Calcined	5.22	5.08	0.0223	1.81
pCN	10.98	11.56	0.0783	2.60
ZnV_2O_6/pCN 100%	11.26	4.80	0.0014	2.21

These observations confirmed successful improvement of pCN/ZnV_2O_6 composite heterojunction.

The growth mechanism of ZnV_2O_6/pCN nanosheets heterojunction is presented in Fig. 5. Owing to the presence of abundant −C−N− motifs in the g-C_3N_4 frame work, g-C_3N_4 could be protonated by HNO_3 easily. This resulted in the surface charge modification to a positively charged surface. Initially, ZnV_2O_6 intermediate with compact nanosheets were formed in large quantity, which might provide the reaction sites and sources for the impending next step [45]. Besides, pCN sheets will be distributed uniformly over the ZnV_2O_6 structure during the growth of 2D sheets. Increasing the reaction time, abundant ZnV_2O_6/pCN sheets were generated by in situ reduction and continuous dissolution of the sheets intermediate product, and simultaneously aggregated into nanosheets to reduce surface energy. As the reaction proceeded in longer time, the nanosheets completely aggregated to regular nanosheets with relatively smooth surface of 2D/2D ZnV_2O_6/pCN heterojunctions.

The morphology of ZnV_2O_6/pCN nanosheets was further examined using TEM as illustrated in Fig. 6. Fig. 6(a) shows the image of ZnV_2O_6 sample prepared after 24 h reaction time, which displays ZnV_2O_6 structure composed of many compact nanosheets. From Fig. 6(b–d) the dark parts should be ZnV_2O_6, while the light parts correspond to pCN, which further demonstrates that pCN nanosheets have covered the surface of ZnV_2O_6 nanosheets. This reveals a good combination of pCN and ZnV_2O_6 to develop heterojunction. The HR-TEM was used to investigate the crystal structure of the pCN combined with ZnV_2O_6 nanosheets, as shown in Fig. 6(e). The interplaner distance was found to be 0.48 and 0.25 nm, which corresponds to (111) and (311) planes of ZnV_2O_6 and pCN, respectively. The SAED pattern of the composite in Fig. 6(f) displays an obvious polycrystalline ring because of good crystallization of ZnV_2O_6.

X-ray photoelectron spectroscopy (XPS) was used to analyze chemical states of the elements in ZnV_2O_6/pCN as shown in Fig. 7. Referring to Fig. 7(a), the XPS survey spectra depicted that the Zn, V, O, C and N elements were detected on the ZnV_2O_6/pCN photocatalysts. Fig. 7(b) exhibits the high-resolution Zn 2p spectrum, in which the binding energies appeared at 1022.3 and 1045.2 eV can be assigned to Zn $2p_{3/2}$ and Zn $2p_{1/2}$, respectively of Zn^{+2} [57]. In addition, two small peaks were also observed with binding energies 1025.5 and 1048.3 eV, which can be ascribed to characteristic of zinc as Zn^o state. The high-resolution V 2p XPS spectrum (Fig. 7c) displays two obvious signals at 517.4 eV (V $2p_{3/2}$) and 524.8 eV (V $2p_{1/2}$), which are typical characteristics of vanadium as V^{5+} [58]. The high-resolution O 1 s XPS spectrum (Fig. 7d) can be resolved into three peaks positioned at 529.6, 531.7 and 534 eV. Peaks located at 529.6 and 531.7 eV can be assigned to the lattice oxygen species in ZnV_2O_6 nanosheets, whereas the peak at 534 eV is attributed to surface-absorbed oxygen species [53]. Two peaks in the range of 284–289 eV have been fitted in the high-resolution C 1 s spectrum in the ZnV_2O_6/pCN composite (Fig. 7e), which ascribed to C−O and C=O species coordinations in graphitic or amorphous carbons adsorbed on the surface [59]. The peak at 290 eV observed in the spectra of ZnV_2O_6/pCN composite can be attributed to the sp^2-bonded C in the N−C−N coordination of g-C_3N_4 [56]. The high-resolution N 1 s spectra showed four deconvolution peaks with binding energies 398.4, 400.3, 401.9 and 405.7 eV (Fig. 7f), indicating four types of N bonding in the samples. The peaks at 398.4 and 400.3 eV were characteristic of the sp^2-bonded aromatic N bound to C atoms in the triazine units (C−N=C) and the bridging N atoms in N-$(C)_3$, respectively [60]. Another peak at 401.9 eV was identified as the terminal amino groups (C−NH) because of incomplete condensation during the thermal polymerization process [61]. The weak peak at 405.7 eV was owing to the successful protonation of g-C_3N_4, rendering the g-C_3N_4 heterocycles positively charged [56].

Fig. 8(a) displays UV–vis diffuse reflectance absorbance spectra of the ZnO/V_2O_5, pCN, ZnV_2O_6/pCN (50%), ZnV_2O_6/pCN (100%), ZnV_2O_6 and ZnV_2O_6 calcined nanosheets. The combined pCN with ZnV_2O_6 nanosheets can obviously enhance the absorbance of pCN towards visible light irradiations. The energy band gaps (E_{bg}) of all the samples were obtained from the extrapolation of Tauc plot to the
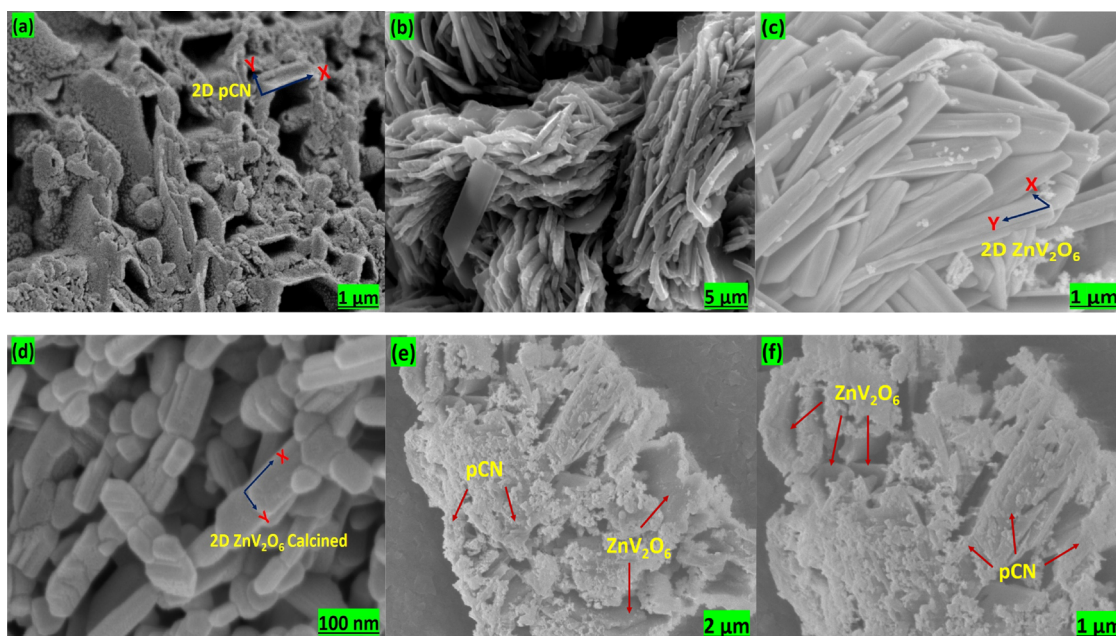

Fig. 3. FE-SEM images of (a) pCN, (b) ZnV_2O_6 after 12 h, (c) ZnV_2O_6 after 24 h, (c) Calcined ZnV_2O_6 after 24 h, (e, f) 2D/2D ZnV_2O_6/pCN (100%).

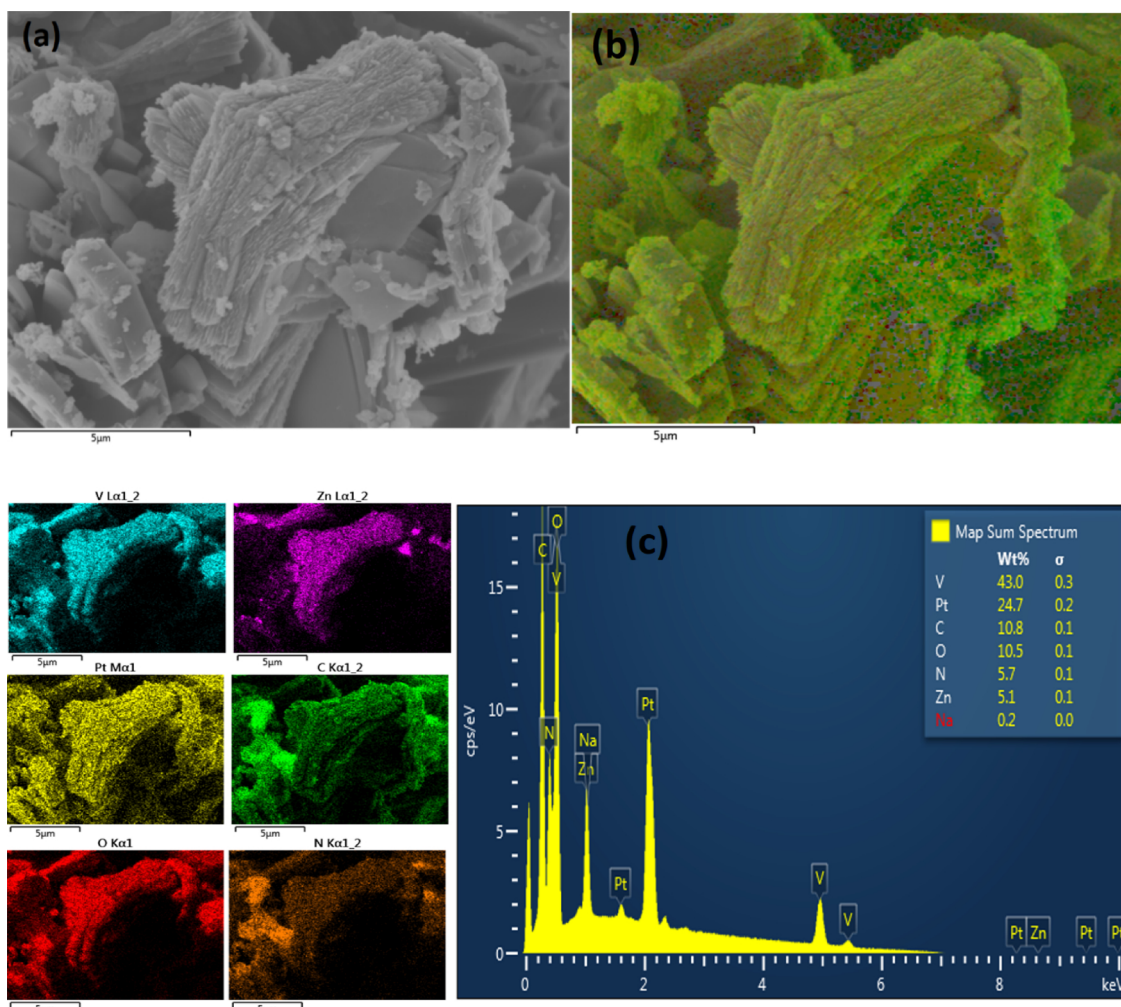**Fig. 4.** EDX mapping analysis of pCN modified ZnV_2O_6 nanosheets: (a) ZnV_2O_6/pCN nanosheets, (b) EDX mapping of ZnV_2O_6/pCN, (c) EDX plots with elements composition.
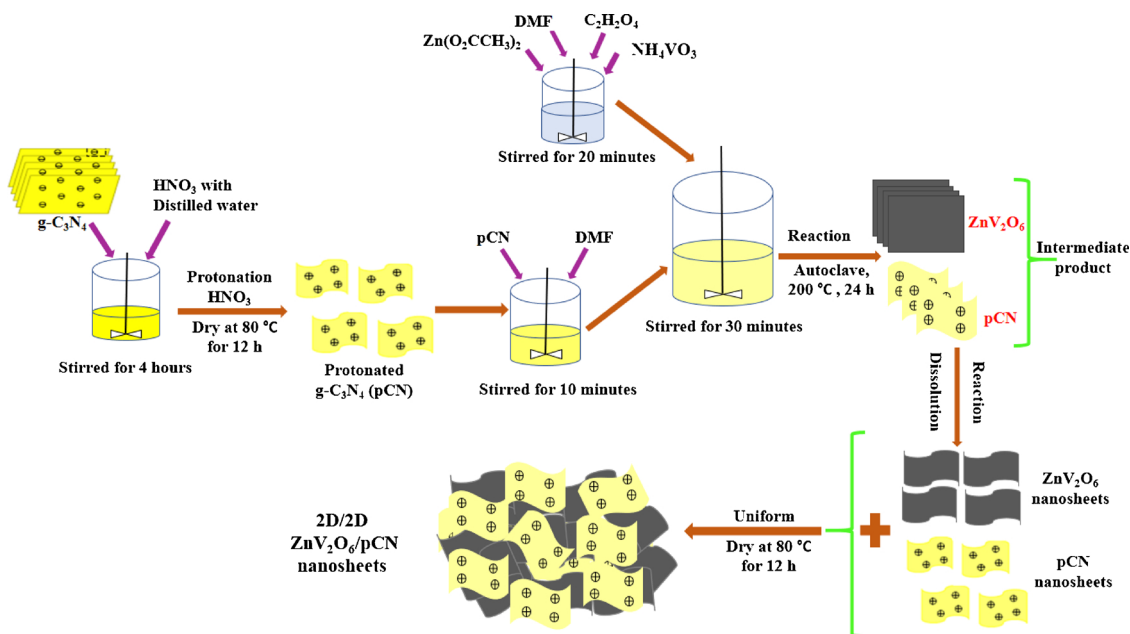

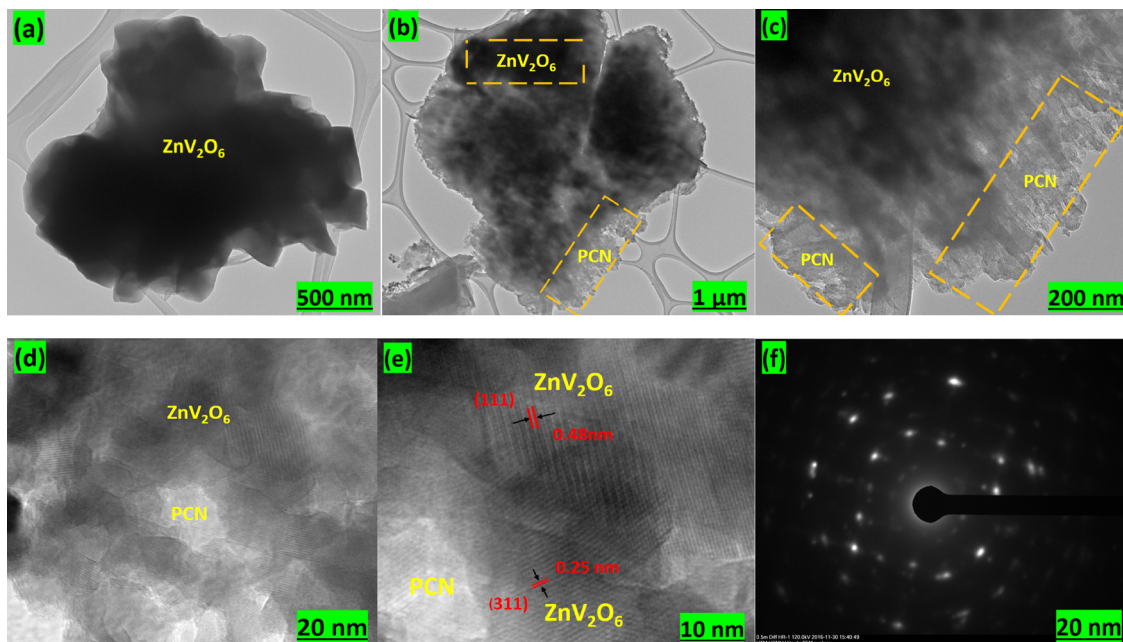**Fig. 5.** Schematic illustration for the formation process of 2D/2D ZnV_2O_6/pCN nanosheets.

Fig. 6. (a) TEM images of 2D ZnV$_2$O$_6$; (b, c, d) TEM images of 2D/2D ZnV$_2$O$_6$/PCN (100%) nanosheets; (e) HR-TEM image of corresponding sample (f) SAED patterns of the sample.

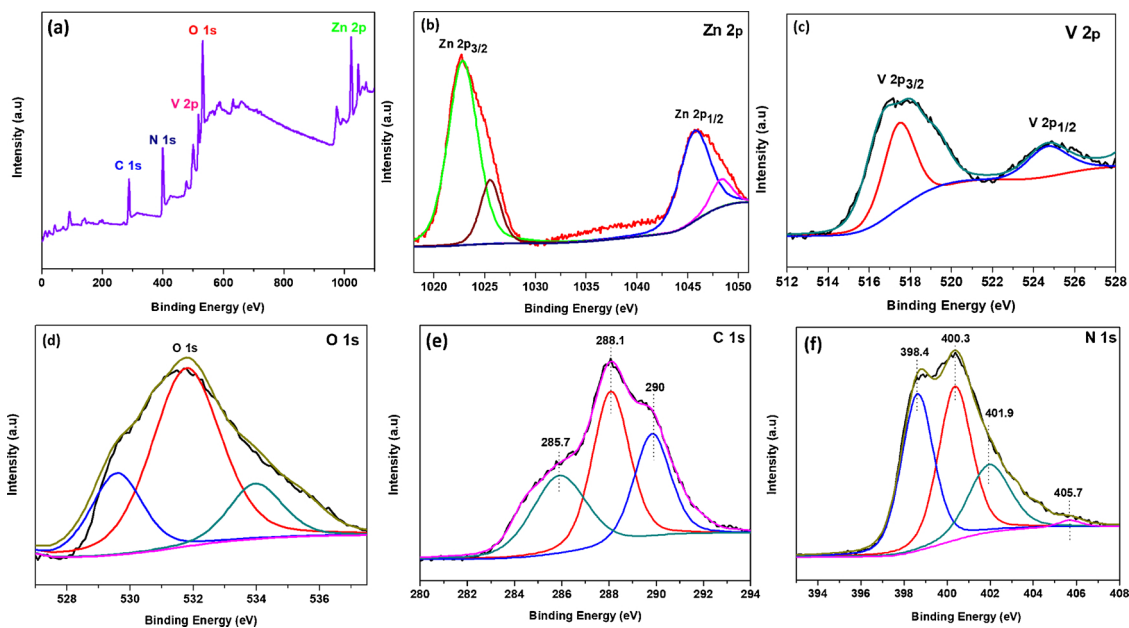**Fig. 7.** XPS spectra of ZnV$_2$O$_6$/PCN (100%): (a) survey spectrum, (b) Zn 2p, (c) V 2p, (d) O 1 s, (e) C 1 s and (f) N 1 s.

abscissa of photon energy (eV). The wavelengths of the ZnO/V$_2$O$_5$, pCN, ZnV$_2$O$_6$/pCN (50%), ZnV$_2$O$_6$/pCN (100%), ZnV$_2$O$_6$ and ZnV$_2$O$_6$ calcined samples are 447, 477, 541, 560, 613 and 685 nm, respectively. Obviously, ZnV$_2$O$_6$ nanosheets shows higher absorption intensities than ZnO/V$_2$O$_5$ composite in the visible light region. Calcining ZnV$_2$O$_6$ nanosheets further shifted absorbance of ZnV$_2$O$_6$ towards higher wavelength of visible light irradiations. The wavelength regions of ZnV$_2$O$_6$/pCN (50%) and ZnV$_2$O$_6$/pCN (100%) composite are extended towards visible-light region compared with the pure pCN. The energy band gaps (E$_{bg}$) of ZnV$_2$O$_6$ and pCN samples were obtained using Tauc plot as shown in Eq. (1).

$$E_g(eV) = \frac{1240}{\lambda} \tag{1}$$

The wavelengths of the ZnV$_2$O$_6$ and pCN photo-catalysts are 613 and 477 nm at which values of E$_g$ for ZnV$_2$O$_6$ and pCN were calculated to be 2.02 and 2.6 eV, respectively. The band position of the conduction bands (E$_{CB}$) of ZnV$_2$O$_6$ and pCN semiconductors were calculated using Eq. (2).

$$E_{VB} = E_{CB} + E_{bg} \tag{2}$$

The valence bands X-ray photoelectron spectroscopy (VB-XPS) were preformed to investigate the VB of ZnV$_2$O$_6$ and pCN. From Fig. 8(b and c), it could be seen that valence band edges of ZnV$_2$O$_6$ and pCN were located at ~1.15 and ~1.48 eV, respectively. The values of E$_{bg}$ for ZnV$_2$O$_6$ and pCN are 2.02 and 2.6 eV, respectively. Therefore, the conduction bands of ZnV$_2$O$_6$ and pCN were calculated to be −0.87 and −1.12 eV, respectively. Thus, it could be concluded that the VB of
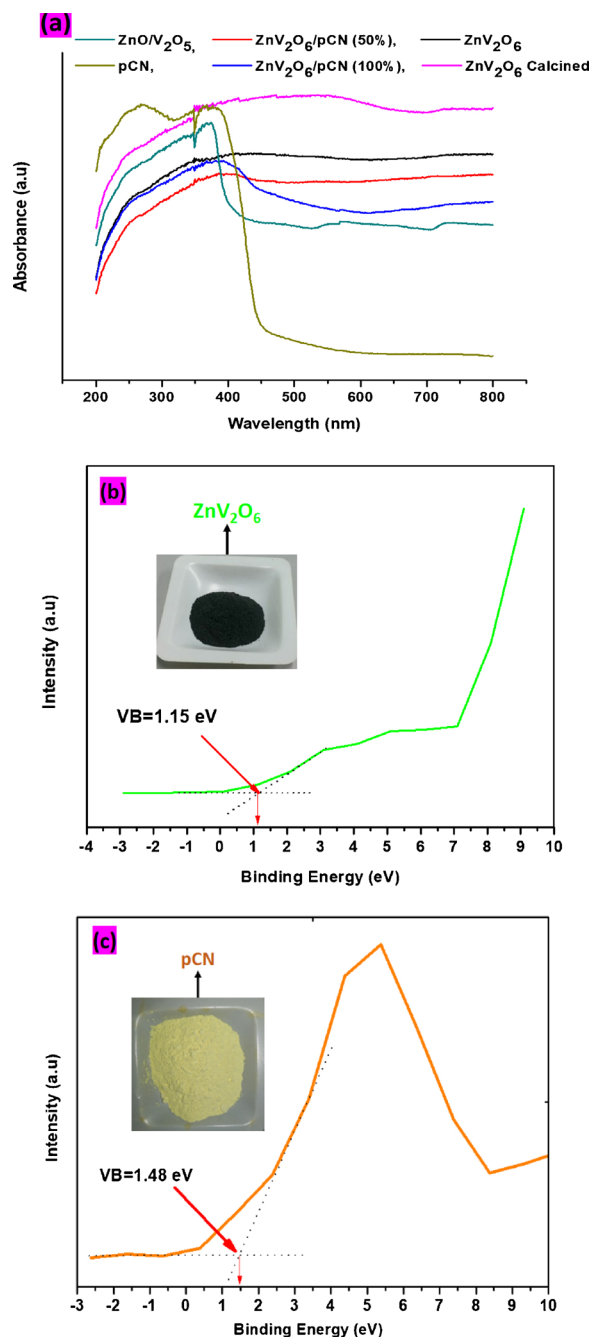
Fig. 8. (a) UV–vis diffuse reflectance absorbance spectra of ZnO/V_2O_5, pCN, 2D ZnV_2O_6, calcined ZnV_2O_6, 2D/2D ZnV_2O_6/pCN (50%) and 2D/2D ZnV_2O_6/pCN (100%) nanosheets; (b) Valence band (VB) XPS spectra of ZnV_2O_6 ; (c) Valence band (VB) XPS spectra of pCN.

ZnV_2O_6 is higher than that of pCN, and the CB of pCN is higher than that of ZnV_2O_6.

Raman spectra of the ZnO/V_2O_5, pCN, ZnV_2O_6, ZnV_2O_6/pCN(50%) and ZnV_2O_6/pCN(100%) nanosheets are depicted in Fig. 9(a). The peaks in the range of 100–1100 cm^{-1} are observed in the pure ZnV_2O_6 and ZnO/V_2O_5 samples. The characteristic peaks of ZnV_2O_6 at 81, 276, 502, 698, 876, 900 and 986 cm^{-1} and the peaks of ZnO/V_2O_5 at 208, 311, 423 and 742 cm^{-1} are observed in the Raman spectrum. Also, the characteristic peaks at 476, 707, 763, 986, 1236 and 1310 cm^{-1} are observed in the Raman spectrum of the pure pCN [55]. Some characteristic bands of the pure ZnV_2O_6 and pCN are found in the Raman spectrum of the ZnV_2O_6/pCN composite. However, several

characteristic peaks of ZnV_2O_6 and pCN are difficult to identify in the ZnV_2O_6/pCN composite, indicating the high dispersion of pCN nanosheets on the surface of the ZnV_2O_6.

Fig. 9(b) illustrates photoluminescence (PL) spectra of the ZnO/V_2O_5, pCN, ZnV_2O_6 calcined, ZnV_2O_6, ZnV_2O_6/pCN(50%), ZnV_2O_6/pCN(100%) and ZnV_2O_6/pCN(150%) samples excited at a wavelength of 325 nm. ZnO/V_2O_5 sample shows a broad PL emission peak at 380 and 510 nm that are composed of emissions because of band gap excitations, the interstitial Zn atoms and the excitations between Zn and singly charges surface oxygen, respectively [62]. These bands, in the order of their appearance are marked as "a" and "b" (Fig. 9b). The ZnV_2O_6 nanosheets display lower PL emission intensity compared with the ZnO/V_2O_5 and ZnV_2O_6 calcined samples. The weaker intensity of the peak represents the lower recombination probability of free charges, which indicates that coupling of vanadium with ZnO to ternary ZnV_2O_6 structure using one-step solvothermal method can effectively mitigate the recombination of photo-generated electron hole pairs. The ZnV_2O_6 calcined shows higher PL emission intensity compared with the ZnV_2O_6 nanosheets because of different phase structure and morphology as evidenced by XRD, BET and FESEM analysis. After the pCN was introduced, the ZnV_2O_6/pCN (50%) and ZnV_2O_6/pCN (100%) nanosheets display lower PL emission intensity compared with the pure ZnV_2O_6 nanosheets. On the other hand, the ZnV_2O_6/pCN (150%) exhibits lower PL emission intensity compared with the ZnV_2O_6/pCN (50%) and ZnV_2O_6/pCN (100%) nanosheets due to increasing the concentration of pCN in composite. The weaker intensity of the peak represents the lower recombination probability of free charges [63]. This indicates that pCN can effectively mitigate the recombination of photo-generated electron hole pairs of ZnV_2O_6 nanosheets.

3.2. Photocatalytic CO_2 reduction with H_2O

For quality assurance and to ascertain correct results, a series of preliminary tests were conducted in the light and catalyst without CO_2 and in the dark with the catalyst and CO_2 under the same experimental conditions. The carbon-based products were not detected in either case. However, a significant amount of methanol was produced during CO_2 reduction with H_2O under the light irradiations in the presence of photocatalyst. These results have confirmed that the photo-reduction products were obtained from the CO_2 source only. All the experiments were repeated at least three times consecutively to check the reliability of the obtained results.

In order to study the effect of reaction medium, the performance of pure $g-C_3N_4$ was tested using water (H_2O) and sodium hydroxide (NaOH) solution and the results are shown in Fig. 10(a). It is obvious that reduction of CO_2 in the presence of 0.1 M NaOH registered high yield of CH_3OH which is 732.9 µ-mol $g-cat^{-1}$ for untreated $g-C_3N_4$, 1.013 fold higher than using pure H_2O. In addition, CH_3OH of 753.7 µmol $g-cat^{-1}$ was obtained over treated $g-C_3N_4$ (pCN), 1.03 times the amount of CH_3OH produced over the untreated $g-C_3N_4$ (732.9 µ-mol $g-cat^{-1}$) in the presence of 0.1 M NaOH. NaOH is able to dissolve and convert more CO_2 compared to the other reaction media. While using H_2O as reductant, the outflow of product gas from the system was more rapid compared to that of NaOH. The CO_2 when dissolved in water only protonates to give CO_3^{2-} ions. In the case of NaOH, the flow of exit gas was slower due to the reaction between CO_2 and NaOH produced HCO_3^- ions. The HCO_3^- was used in the production of CH_3OH after it received photogenerated electrons on the catalysts surface. In addition, highly concentrated OH^- ions in the aqueous solution act as strong holes scavengers and forms OH radicals. This consequently leads to more utilization of surface electrons that stimulates reduction of CO_2 to CH_3OH. With respect to the catalyst treatment, treated $g-C_3N_4$ recorded higher yield of methanol compared to untreated $g-C_3N_4$ under the same reaction medium. The protonation of $g-C_3N_4$ leads to exfoliation on the structures and forms ultra-small pores. This aids in the higher separation and transfer efficiency of the photo-
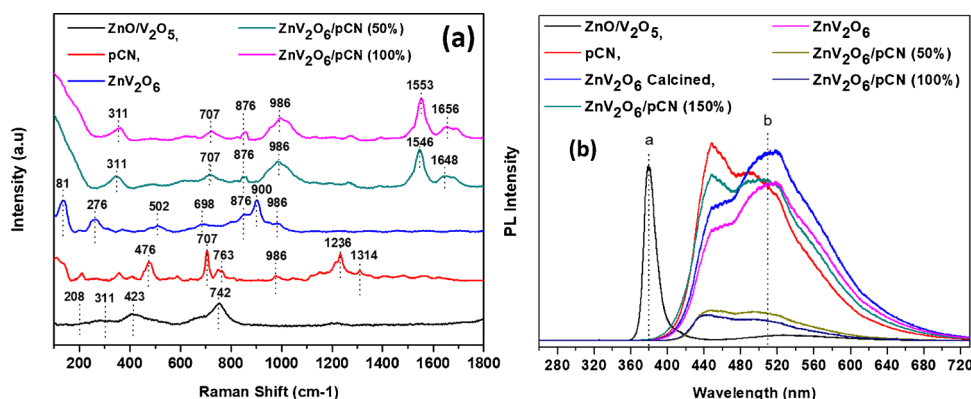
Fig. 9. (a) Raman spectra of ZnO/V_2O_5, pCN, ZnV_2O_6, ZnV_2O_6/pCN (50%) and ZnV_2O_6/pCN (100%) nanosheets; (b) Photoluminescence (PL) spectra for ZnO/V_2O_5, pCN, ZnV_2O_6, calcined ZnV_2O_6, ZnV_2O_6/pCN (50%), ZnV_2O_6/pCN (100%) and ZnV_2O_6/pCN (150%) nanosheets.

generated electrons and holes.

Fig. 10(b) shows the effect of different photo-catalysts such as ZnO, V_2O_5, ZnO/V_2O_5, ZnV_2O_6 and ZnV_2O_6 calcined on the photoactivity for dynamic CO_2 conversion with 0.1 M NaOH solution under visible light irradiation. The effectiveness of the catalyst samples was analysed based on the yield of CH_3OH. Pure ZnO, V_2O_5 and ZnO/V_2O_5 nanocatalyst synthesized by the sol-gel method scarcely reduced CO_2 and displayed very poor activity for CH_3OH formation. However, the production of CH_3OH was significantly enhanced using hierarchical 2D ZnV_2O_6 nanosheets because of efficient visible light absorption, efficient charge transfer property and higher electron mobility with hindered recombination rate by some amount of V_2O_5 in the sample as evidenced by XRD analysis [64]. More importantly, ZnV_2O_6 calcined at 550 °C for 3 h displayed poor activity under the same operating conditions. According to PL emission spectra and BET surface area, the calcined ZnV_2O_6 sample displays higher PL emission intensity and lower surface area compared with the bare ZnV_2O_6 nanosheets. Recently, Zhang et al. [54] reported similar observations while investigating hydrogen evolution from water over $BiFeO_3$, $Bi_2Fe_4O_9$ and $BiFeO_3/Bi_2Fe_4O_9$ heterojunction nanofibers under visible light irradiation. Thus, lower photo-activity of calcined ZnV_2O_6 sample was possibly because of reduction of ZnV_2O_6 at elevated temperature with

different phase structure and much lower band gap energy (Ebg = 1.81 eV).

Fig. 10(c) displays the effect of different catalyst preparation times of 12, 24, 48 and 72 h at one fixed temperature (200 °C) for the prepared ZnV_2O_6 catalysts for photoreduction of CO_2 with H_2O under visible light irradiation in reaction medium (Room temperature, atmospheric pressure, feed flow rate 20 mL/min and irradiation time = 2 h). The result exhibits that the effect of exposure time of heating for 24 h for prepared ZnV_2O_6 sample shows much higher CH_3OH evolution rate than heating time for 12 h. However, catalyst preparation time of 48 and 72 h have no significant effect on production rate. Thus, ZnV_2O_6 samples prepared at exposure time of 24 h were further used to investigate the effect of irradiation time and stability analysis.

The effect of pCN on the performance of ZnV_2O_6 for photocatalytic CO_2 reduction with H_2O to CH_3OH under visible light irradiations is illustrated in Fig. 10(d). It can be seen that the yield of CH_3OH over ZnV_2O_6 was higher than that over pCN, which can be ascribed to the better photoabsorption performance, higher surface area and larger average pore diameter of ZnV_2O_6 compared with pCN. It also can be noticed that the generation rates of CH_3OH over the ZnV_2O_6/pCN composite were significantly higher than that over ZnV_2O_6 or pCN under visible light irradiation. Combined pCN with ZnV_2O_6 has
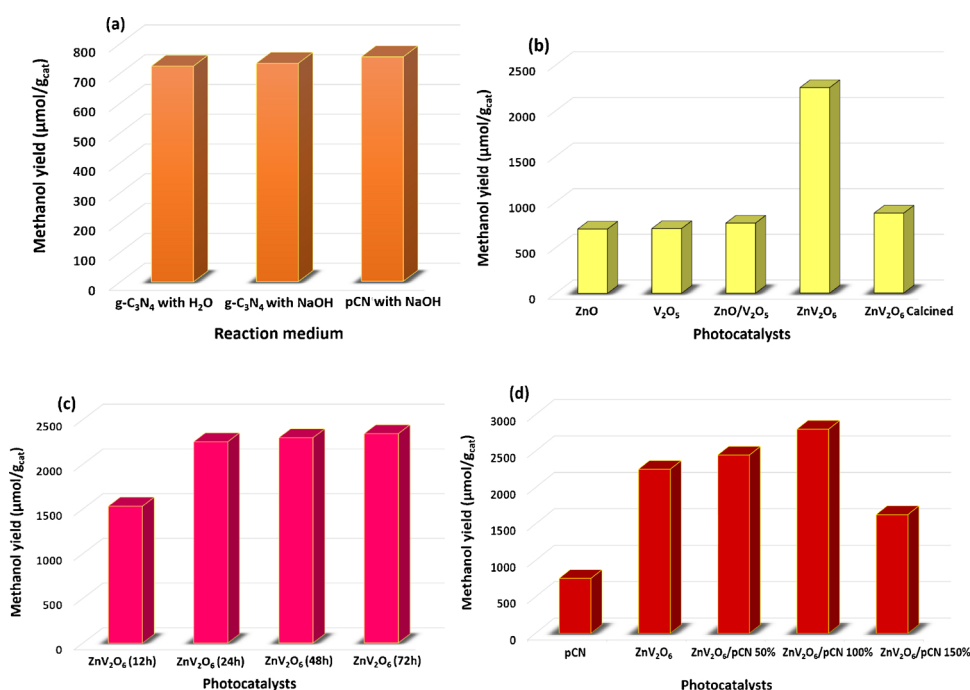

Fig. 10. (a) Yield of methanol for different reaction mediums; (b) Effect of types of photo-catalysts on yield of methanol; (c) Effect of different exposure times of heating for 12, 24, 48 and 72 h for prepared ZnV_2O_6 catalyst for CO_2 photo reduction (d) Yield of methanol over various photo-catalysts: reaction parameters (Room temperature, atmospheric pressure, feed flow rate 20 ml/min and irradiation time 2 h).
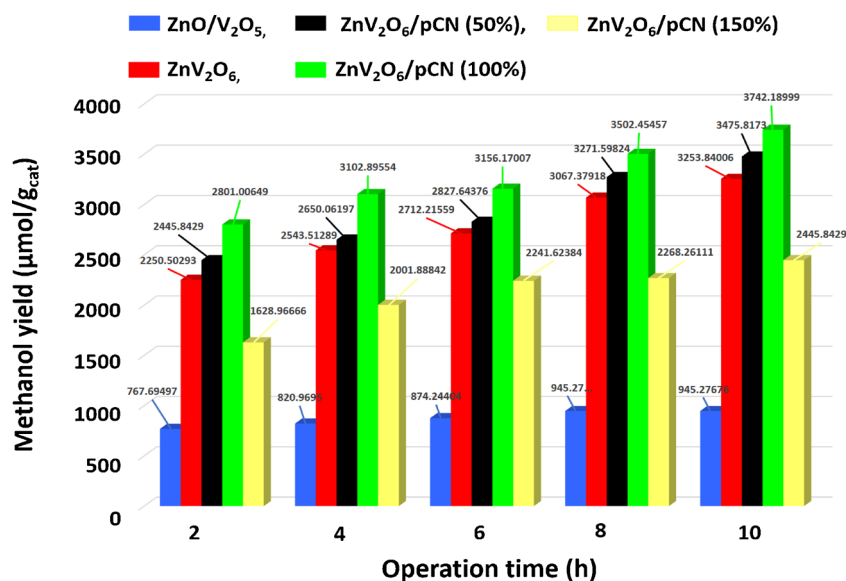
Fig. 11. Effect of pCN on the photoactivity on ZnV_2O_6 for CO_2 photo-reduction to CH_3OH at different irradiation times (100 mg catalyst, 100 mL distilled water with 0.1 M NaOH, room temperature, atmospheric pressure, and feed flow rate 20 mL/min).

significantly improved CO_2 photoreduction and the composite ratios 1:1 gives the optimal yield of CH_3OH. In general, significantly enhanced photoactivity of pCN combined with ZnV_2O_6 nanosheets towards CO_2 reduction was evidently because of the heterojunction structures, which improves the separation of electrons and holds, prevents the charge-carrier recombination and prolongs the lifetime of photo-carriers in ZnV_2O_6/pCN photocatalysts.

Further investigations were carried out to study the effect of irradiation time on dynamic photocatalytic reduction of CO_2 in a slurry photoreactor. Fig. 11 displays the photocatalytic CH_3OH evolution using ZnO/V_2O_5, ZnV_2O_6 and ZnV_2O_6/pCN composite with different molar ratios under visible light irradiation. It can be seen that, without pCN, pure ZnO/V_2O_5 and ZnV_2O_6 samples have a lower property on CH_3OH generation in the photocatalytic CO_2 reduction compared with ZnV_2O_6/pCN composite. After irradiation time of 10 h, the CH_3OH yield of ZnV_2O_6/100%pCN (3742.19 μmol g-cat^{-1}) was about 4 times higher than that of pure ZnO/V_2O_5 (945.28 μmol g-cat^{-1}) and 1.15 times higher than that of pure ZnV_2O_6 (3253.84 μmol g-cat^{-1}). However, production of CH_3OH was significantly enhanced using ZnV_2O_6/pCN 2D/2D nanosheets heterojunction because of synergistic effects, efficient visible light absorption, appropriate band structure and higher electron mobility by a mediator with hindered recombination rate.

The efficiency of pCN modified ZnV_2O_6 nanosheets was further examined based on the quantum yield, calculated for each experiment, as the ratio of the product rate (mole per sec) with photonic flux (mole per sec). The quantum yield of CO_2 photo-reduction can be defined as the ratio of amount of products (mole per sec) with photonic flux (mole per sec) as explained in Eq. (3) [65].

$$Quantum\ yield = \frac{n \times production\ rate(mol/sec)}{moles\ of\ photon\ flux(mol/sec)} \tag{3}$$

The quantum yield was calculated based on 6, 2, 8 and 2 electrons (n) used for CH_3OH, CO, CH_4 and H_2 production rate, respectively and moles of photon input energy over the ZnV_2O_6/pCN (100%) as displayed in Table 2. The effects of Visible- light, UV-light and solar-light irradiations on the photo-activity of ZnV_2O_6/pCN nanosheets catalyst were investigated using liquid phase and gas phase photocatalytic systems. The significantly enhanced Quantum yield for CH_3OH could be seen over visible-light in liquid phase compared to UV-light and Solar-Light irradiations in gas phase. Over the visible-light, the quantum efficiency of CH_3OH production was 0.081, 38.6 times higher than over

Table 2
Summary of yield rates and quantum yield over ZnV_2O_6/pCN (100%).

System	Yield rate (μmol g-cat.$^{-1}$ h^{-1}) [a]				Quantum yield			
	CH_3OH	CO	CH_4	H_2	CH_3OH	CO	CH_4	H_2
Liquid phase [b]	776	–	–	–	0.081	–	–	–
Gas Phase [c]	14	443	71	64	0.0014	0.015	0.0098	0.0022
Gas Phase [d]	20	809	14	85	0.0021	0.028	0.0019	0.0029

[a] Yield rates calculated at 4 h irradiation.
[b] Liquid phase, Visible-Light, 20 mW cm^{-2}, 450 nm.
[c] Gas phase, UV-Light, 150 mW cm^{-2}, 254 nm.
[d] Gas phase, Visible-light, 100 mW cm^{-2}, 450 nm.

solar-light and 57.9 times higher than over UV-Light irradiations. The quantum efficiencies of CH_3OH, CO and H_2 production over solar-light in gas phase were 0.0021, 0.028 and 0.0029, respectively. By comparing the performance of solar-light, the efficiency of solar-light was higher than UV-Light irradiations. On the other hand, the quantum efficiency for CH_4 production was 0.0098 over UV-light, 5.1 times larger than over solar-light irradiations. The significantly enhanced quantum yield over ZnV_2O_6/pCN (100%) was evidently because of efficient charge transfer rate and higher electron mobility by a mediator.

The effects of UV-light and solar-light irradiations on the photo-activity of ZnV_2O_6 combined with pCN nanosheets catalyst were investigated using gas phase photocatalytic system. Fig. 12(a) shows the continuous production of CO over ZnV_2O_6 combined with pCN under UV-light and solar-light irradiation at different reaction times. Evidently, different amounts of CO were produced during photo-induced CO_2 reactions under UV-light and solar-light of different intensities. The solar-light irradiation can produce more electron-hole pairs over the ZnV_2O_6 surface due to appropriate band structure. Therefore, the production of CO as the main product was found to be higher using solar-light irradiation.

The photocatalytic reduction of CO_2 to H_2 under UV-light and solar-light is depicted in Fig. 12(b). The production of H_2 was significant using solar simulated light which revealed that solar light is encouraging for the production of H_2. In the case of visible light, the yield of H_2 gradually increased until reached to steady state in the entire irradiation period. While in the case of UV-light, the yield of H_2 gradually increased at the beginning and then decreased significantly after two
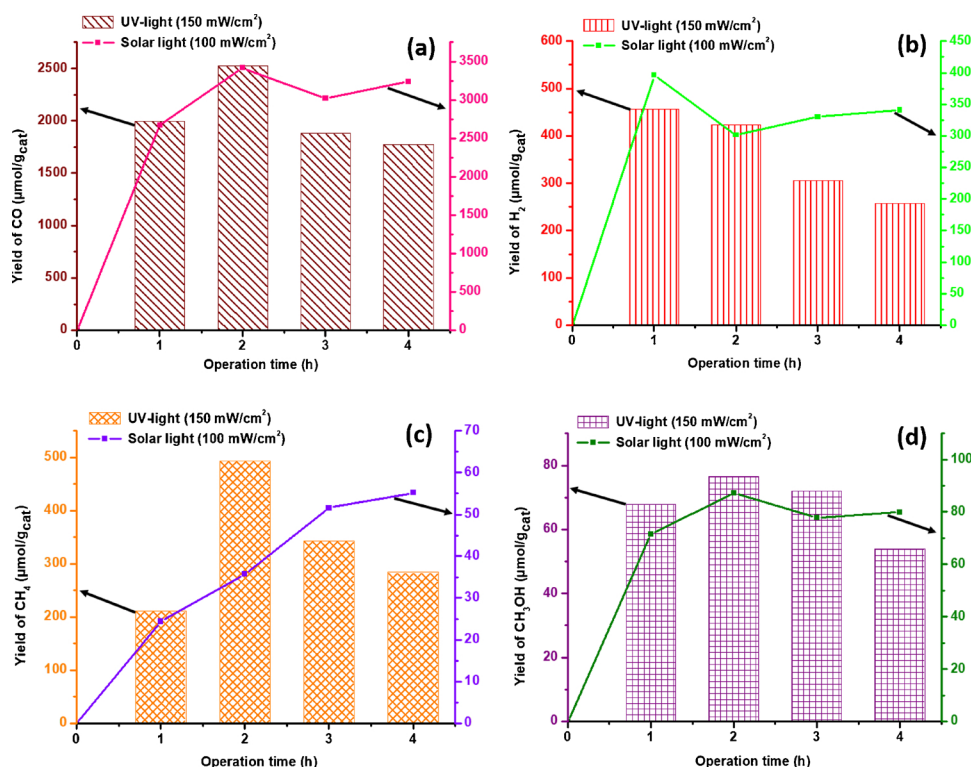
Fig. 12. Effect of irradiation time against products yield over ZnV_2O_6/pCN composite (a) Yield of CO for UV and solar light against irradiation time; (b) Yield of H_2 for UV and solar light against irradiation time; (c) Yield of CH_4 for UV and solar light against irradiation time; (d) Yield of CH_3OH for UV and visible light against irradiation time.

hours. Initially, the UV-light irradiation can produce more electron-hole pairs over the ZnV_2O_6/pCN surface due to higher photon energy ($150\,mW/cm^2$). Therefore, the production of H_2 were maximum. The decreased in H_2 production over the irradiation time would probably be due to increasing reaction temperature because of higher photon energy ($150\,mW/cm^2$). At elevated temperature, there would be less adsorption of reactants over the catalyst surface, resulting in reduced productivity.

Fig. 12(c) displays the continuous production of CH_4 over ZnV_2O_6 combined with g-C_3N_4 under UV-light and solar-light irradiation at different reaction times. Noticeably, the CH_4 yield was decreased gradually over the irradiation time under UV-light irradiation, while it was increased significantly under solar-light irradiation. However, photoactivity of ZnV_2O_6/pCN nanosheets was very stable under solar-light irradiation ($100\,mW/cm^2$). This has confirmed prolonged photoactivity of ZnV_2O_6/pCN nanosheets for continuous CH_4 production under solar-light.

The photocatalytic CO_2 reduction to CH_3OH for ZnV_2O_6/pCN nanosheets catalyst is presented in Fig. 12(d). the CH_3OH production increased significantly at the start of the run and then gradually decreased over the irradiation time. However, ZnV_2O_6/pCN nanosheets catalyst found efficient for continuous production of CH_3OH under solar-light irradiation. While in the case of UV-light, yiled rate was declined because of less adsorption of reactants over the catalyst surface due to increasing reaction temperature caused by photon energy ($150\,mW/cm^2$). In general, significantly enhanced photoactivity of ZnV_2O_6/pCN nanosheets toward CO_2 reduction was evidently due to synergistic effects, efficient visible light absorption, appropriate band structure and higher electron mobility with hindered recombination rate.

The performance of ZnV_2O_6/pCN 2D/2D nanosheets was further compared with the results reported by previous researchers as depicted in Table 3. CO_2 was converted to CH_3OH using $CdIn_2S_4$/g-C_3N_4 and a yield of $42.7\,\mu mol\,g\text{-cat}^{-1}$ obtained after 1 h reaction time [66]. ZnO-rGO was used for CO_2 photo-reduction, with the maximum CH_3OH yield of $263.1\,\mu mol\,g\text{-cat}^{-1}$ obtained after 3 h [67]. Similarly, Bi_2S_3/

CdS gave CH_3OH yield of $613\,\mu mol\,g\text{-cat}^{-1}$ after 5 h during CO_2 photo-reduction with H_2O [68]. ZnO/ZnSe were used to convert CO_2 to CH_3OH and reported optimum yield of $1581.82\,\mu mol\,g\text{-cat}^{-1}$ after 1 h [69]. The superior yield of CH_3OH obtained in the present study using ZnV_2O_6/pCN 2D/2D nanosheets can be assigned to the visible light absorption property of ZnV_2O_6 as a result of its suitable band gap, the ability of protonated g-C_3N_4 as a mediator to act as an electron trapping agent, whilst maintaining mobility of photo-generated electrons and the synergistic interaction between the constituents of the composite.

The stability of ZnV_2O_6 and ZnV_2O_6/pCN (100%) nanosheets catalyst was further investigated to evaluate the life of catalyst in a slurry photoreactor under visible light irradiations. The photo-stability test was performed with a cumulative of 32 h irradiation time. The effects of pCN combined with ZnV_2O_6 for photocatalytic CO_2 reduction with H_2O to CH_3OH using different irradiation times at atmospheric pressure, room temperature and feed flow rate $20\,mL/min$ are illustrated in Fig. 13(a). The production of CH_3OH concentration gradually increased until reached to steady state. More importantly, catalyst sustained photo-stability even after 32 h of irradiation for selective production of CH_3OH. Thus, visible light can be considered more effective and efficient for photoreduction of CO_2 to CH_3OH using ZnV_2O_6/pCN composite as it gave the highest yield of both products and demonstrated better stability. The ZnV_2O_6/pCN composite combined the strengths of ZnV_2O_6 and pCN. This interaction in the heterostructure improved its photocatalytic activity.

Fig. 13(b) shows the schematic for photocatalytic process for CO_2 reduction with H_2O over ZnV_2O_6, ZnV_2O_6/g-C_3N_4 and ZnV_2O_6/pCN nanosheets under visible light irradiation. The 2D ZnV_2O_6 nanosheets provide higher photoactivity and stability for enhanced CO_2 reduction to CH_3OH. The addition of pCN further developed the photo-activity due to strong visible light absorption because of synergistic effect between ZnV_2O_6/pCN nanosheets. Moreover, surface charge modification via protonation of graphitic carbon nitride (g-C_3N_4) can serve as a mediator for electron trapping. This can greatly promote the production and separation of photo-generated carriers under the broader visible light spectrum.

Table 3
Summary of products yield rates during photocatalytic CO_2 reduction using different catalysts.

Catalysts	Yield (μmol g-cat^{-1}) CH_3OH	Light Source	Catalyst Used (g)	Ref.
ZnV_2O_6/pCN	3742	35 W HID Xe lamp, 20 mWcm^{-2}	0.1	Current Study
$CdIn_2S_4$/g-C_3N_4	427	300 W xenon lamp	0.1	[66]
ZnO/rGO	263	300 W Xenon lamp	0.1	[67]
Bi_2S_3/CdS	3065	500 W Xe lamp	0.2	[68]
ZnO/ZnSe	1582	250 W high-pressure mercury lamp	0.02	[69]
CuO/$NaTaO_3$	1909	250 W high-pressure mercury lamp	0.012	[70]
CdS(Bi_2S_3)/TiO_2	1123	500 W Xe lamp	0.2	[71]

3.3. Mechanism of reaction

Mechanism of reaction electron (e$^-$) and hole (h$^+$) are generated during the photocatalytic process, when the light strike over the 2D/2D ZnV_2O_6/pCN surface. The holes can oxidize H_2O while the photo-excited electrons can reduce CO_2 to form CH_3OH, CO, CH_4 and H_2. The reactions in Eqs. (4)–(12) may express the pathways in CO_2 photo-reduction to solar fuels.

$$ZnV_2O_6 + hv \rightarrow h^+ + e^- \tag{4}$$

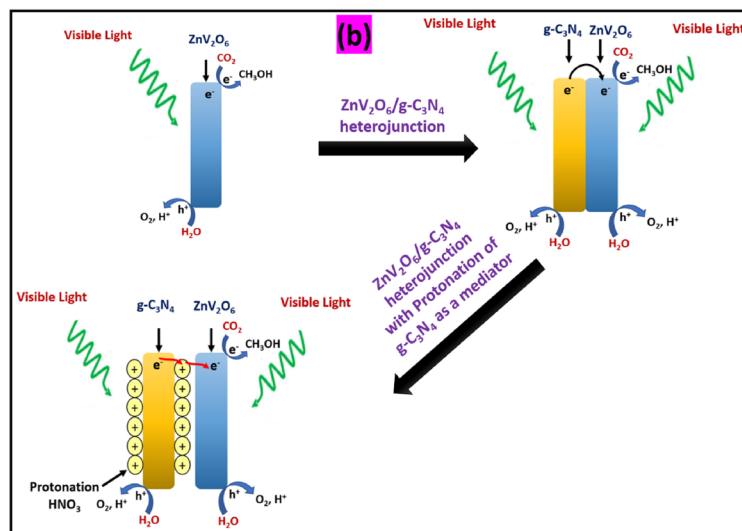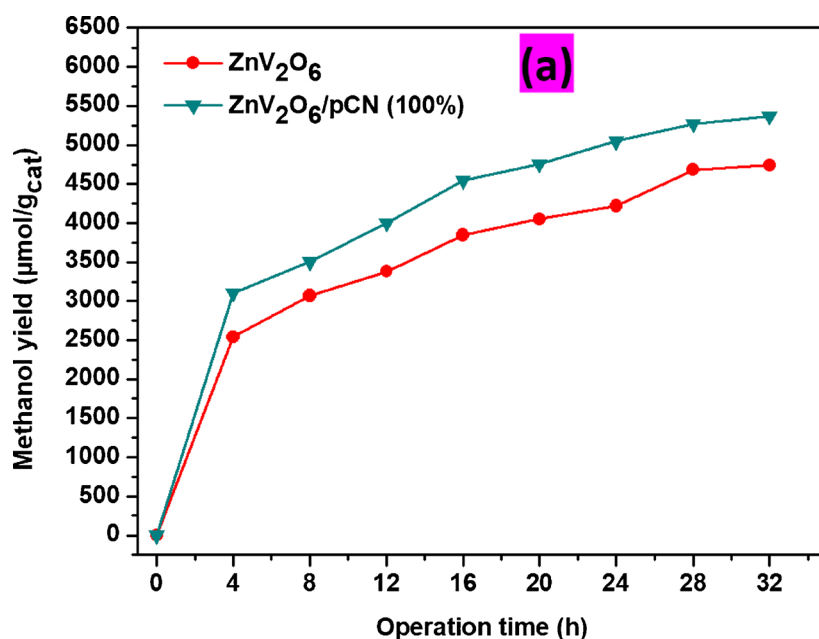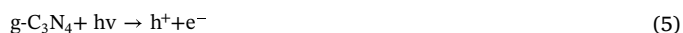$$\text{g-}C_3N_4 + hv \rightarrow h^+ + e^- \tag{5}$$

Fig. 13. (a) Stability study under visible light irradiation of ZnV_2O_6 and ZnV_2O_6/pCN (100%) nanosheets catalyst for CO_2 reduction to CH_3OH; (b) Proposed mechanism showing a photocatalytic process for CO_2 reduction by H_2O to CH_3OH on ZnV_2O_6, ZnV_2O_6/g-C_3N_4 and ZnV_2O_6/pCN nanosheets under visible light irradiation.
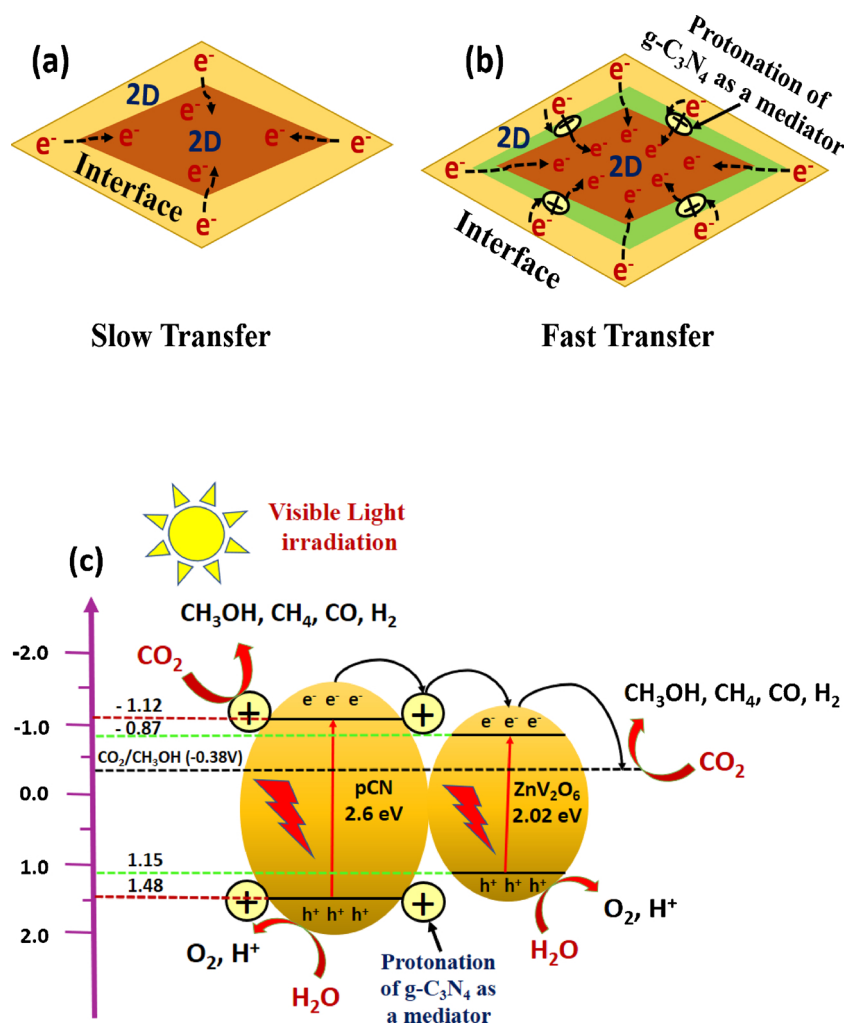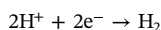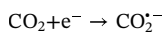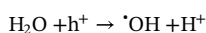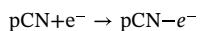
Fig. 14. Schematic illustration of contact interfaces for (a) 2D/2D heterojunction and (b) 2D/2D heterojunction with protonation (HNO₃) as a mediator. (c) Schematic diagram of the separation and transfer of photogenerated charges in ZnV_2O_6/pCN composite under visible light irradiation.

$$pCN + e^- \rightarrow pCN - e^- \tag{6}$$

$$H_2O + h^+ \rightarrow {}^{\bullet}OH + H^+ \tag{7}$$

$$CO_2 + e^- \rightarrow CO_2^{\bullet-} \tag{8}$$

$$2H^+ + 2e^- \rightarrow H_2 \tag{9}$$

$$CO_2 + 2H^+ + 2e^- \rightarrow CO + H_2O \tag{10}$$

$$CO_2 + 6H^+ + 6e^- \rightarrow CH_3OH + H_2O \tag{11}$$

$$CO_2 + 8H^+ + 8e^- \rightarrow CH_4 + H_2O \tag{12}$$
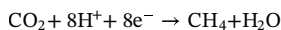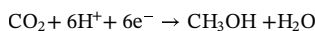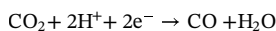
Eqs. (4)–(6) reveals photo-excited electron-hole pairs production and their trapping by surface charge modification and heterojunctions, thus increasing the lifetime of charges to precede oxidation and reduction process. Reduction of CO_2 occurs at the CB by the activity of electrons and H_2O is oxidized by holes at the VB and this is kinetically explained in Eqs. (7) and (8). The production of H_2, CO, CH_3OH and CH_4 through the photoreduction of CO_2 is shown in Eqs. (9)–(12).

The schematic of contact interfaces is illustrated in Fig. 14(a and b). When g-C_3N_4 nanosheets have grown on the surfaces of ZnV_2O_6 nanosheets in the face-to-face way, and only a small quantity of charge transfer nanochannels can be generated in the 2D/2D ZnV_2O_6/g-C_3N_4 sample (Fig. 14a), resulting in a slow charge transport efficiency and limited photocatalytic activity. However, the uniformly distributed protonated g-C_3N_4 (pCN) nanosheets on ZnV_2O_6 nanosheets with face-to-face contact way can construct plentiful high-speed charge transfer

nanochannels (Fig. 14b), which strongly accelerate the high-efficiency separation and migration for the photogenerated charges. The protonation of graphitic carbon nitride (g-C_3N_4) can serve as a mediator and trap for photoexcited electrons. Based on the above analysis, it is confidently concluded that the outstanding photocatalytic activity of 2D/2D ZnV_2O_6/pCN nanosheets heterojunction is mainly derived from the high photo-induced charge separation and migration efficiency by the formation of well-designed high-speed charge transfer nanochannels with a mediator.

On the basis of the above discussion, a visible-light photocatalytic reduction of CO_2 mechanism over the ZnV_2O_6/pCN sample was delineated in Fig. 14(c). The pCN in the heterostructured photocatalysts acts as a sensitizer to absorb photons as well as excite electron and hole pairs upon light irradiation. Since the CB edge potential of pCN (-1.12 eV) is more negative than that of ZnV_2O_6 (-0.87 eV), the photoexcited electrons on pCN could transfer to the CB of ZnV_2O_6. Surface charge modification through protonation of graphitic carbon nitride (g-C_3N_4) can serve as an excellent acceptor and trap for photoexcited electrons; hence the photoinduced electrons could be quickly transferred to the ZnV_2O_6 to generate CH_3OH, CO, CH_4 and H_2. In such a way, the photoexcited electron–hole pairs could be effectively separated. Hence, the formed the junction between pCN and ZnV_2O_6 in the heterostructured photocatalysts would suppress the recombination of electrons and holes in carriers–transfer process and thus results in an enhanced photocatalytic activity of pCN/ZnV_2O_6 heterojunctions.

4. Conclusions

The combining pCN with ZnV_2O_6 2D/2D nanosheets heterojunction was successfully investigated in liquid and gas phase systems for selective CO_2 photoreduction with H_2O to CH_3OH, CO, CH_4 and H_2 under UV and visible light irradiations. The enhanced photoactivity and performance of the nanocomposite can be attributed to the arrangement of the constituents of the composite which affected the mechanism of the photoreaction as well as a mediator for electron trapping. The interaction between ZnV_2O_6 and pCN combined in the appropriate ratio is another reason for the effectiveness of the composite. The combined efforts of both constituents helped to overcome limitations of the other hence deploying their fortes. Using slurry system, the maximum yield of CH_3OH product over ZnV_2O_6/100 wt% pCN catalyst was 3742.19 µmol g-cat^{-1}, significantly higher than using ZnV_2O_6 and pCN under visible light irradiation. In addition, the yield rate of CO as a main product over ZnV_2O_6/pCN nanosheets was 3237 µmol g-cat^{-1} using gas phase system. Stability test confirmed prolonged stability of ZnV_2O_6/pCN nanosheets for selective CH_3OH production under visible light irradiations. The ZnV_2O_6/pCN composite combined the strengths of ZnV_2O_6 and pCN. This interaction in the heterostructure generally developed its photocatalytic activity making it a suitable visible light photocatalyst for effective CO_2 photo-reduction.

Acknowledgements

References

[1] Z. Sun, H. Wang, Z. Wu, L. Wang, g-C$_3$N$_4$ based composite photocatalysts for photocatalytic CO$_2$ reduction, Catal. Today 300 (2018) 160–172.

[2] M. Tahir, B. Tahir, N.A.S. Amin, H. Alias, Selective photocatalytic reduction of CO$_2$ by H$_2$O/H$_2$ to CH$_4$ and CH$_3$OH over Cu-promoted In$_2$O$_3$/TiO$_2$ nanocatalyst, Appl. Surf. Sci. 389 (2016) 46–55.

[3] L. Lin, C. Hou, X. Zhang, Y. Wang, Y. Chen, T. He, Highly efficient visible-light driven photocatalytic reduction of CO$_2$ over g-C$_3$N$_4$ nanosheets/tetra (4-carbox-yphenyl) porphyrin iron (III) chloride heterogeneous catalysts, Appl. Catal. B 221 (2018) 312–319.

[4] Z. Xiong, Z. Lei, C.-C. Kuang, X. Chen, B. Gong, Y. Zhao, J. Zhang, C. Zheng, J.C. Wu, Selective photocatalytic reduction of CO$_2$ into CH$_4$ over Pt-Cu$_2$O TiO$_2$ nanocrystals: The interaction between Pt and Cu$_2$O cocatalysts, Appl. Catal. B 202 (2017) 695–703.

[5] W. Li, Y. Shi, Y. Luo, Y. Wang, N. Cai, Carbon monoxide/carbon dioxide electro-chemical conversion on patterned nickel electrodes operating in fuel cell and electrolysis cell modes, Int. J. Hydrogen Energy 41 (2016) 3762–3773.

[6] T. Inoue, A. Fujishima, S. Konishi, K. Honda, Photoelectrocatalytic reduction of carbon dioxide in aqueous suspensions of semiconductor powders, Nature 277 (1979) 637–638.

[7] M. Tahir, Synergistic effect in MMT-dispersed Au/TiO$_2$ monolithic nanocatalyst for plasmon-absorption and metallic interband transitions dynamic CO$_2$ photo-reduction to CO, Appl. Catal. B 219 (2017) 329–343.

[8] Q. Wang, W. Wang, B. Yan, W. Shi, F. Cui, C. Wang, Well-dispersed Pd-Cu bimetals in TiO$_2$ nanofiber matrix with enhanced activity and selectivity for nitrate catalytic reduction, Chem. Eng. J. 326 (2017) 182–191.

[9] J. Low, B. Cheng, J. Yu, Surface modification and enhanced photocatalytic CO$_2$ reduction performance of TiO$_2$: a review, Appl. Surf. Sci. 392 (2017) 658–686.

[10] N. Shehzad, M. Tahir, K. Johari, T. Murugesan, M. Hussain, A critical review on TiO$_2$ based photocatalytic CO$_2$ reduction system: strategies to improve efficiency, J. CO$_2$ Util. 26 (2018) 98–122.

[11] T.M. Suzuki, T. Nakamura, S. Saeki, Y. Matsuoka, H. Tanaka, K. Yano, T. Kajino, T. Morikawa, Visible light-sensitive mesoporous N-doped Ta$_2$O$_5$ spheres: synthesis and photocatalytic activity for hydrogen evolution and CO$_2$ reduction, J. Mater. Chem. 22 (2012) 24584–24590.

[12] N. Matinise, X. Fuku, K. Kaviyarasu, N. Mayedwa, M. Maaza, ZnO nanoparticles via moringa oleifera green synthesis: physical properties & mechanism of formation, Appl. Surf. Sci. 406 (2017) 339–347.

[13] G. Mahmodi, S. Sharifnia, F. Rahimpour, S. Hosseini, Photocatalytic conversion of CO$_2$ and CH$_4$ using ZnO coated mesh: effect of operational parameters and opti-mization, Sol. Energy Mater. Sol. Cells 111 (2013) 31–40.

[14] Y.S. Chaudhary, T.W. Woolerton, C.S. Allen, J.H. Warner, E. Pierce, S.W. Ragsdale, F.A. Armstrong, Visible light-driven CO$_2$ reduction by enzyme coupled CdS nanocrystals, Chem. Commun. 48 (2012) 58–60.

[15] S. Cao, Y. Li, B. Zhu, M. Jaroniec, J. Yu, Facet effect of Pd cocatalyst on photocatalytic CO$_2$ reduction over g-C$_3$N$_4$, J. Catal. 349 (2017) 208–217.

[16] J. Lv, K. Dai, J. Zhang, Q. Liu, C. Liang, G. Zhu, Facile constructing novel 2D porous g-C$_3$N$_4$/BiOBr hybrid with enhanced visible-light-driven photocatalytic activity, Sep. Purif. Technol. 178 (2017) 6–17.

[17] G. Shi, L. Yang, Z. Liu, X. Chen, J. Zhou, Y. Yu, Photocatalytic reduction of CO$_2$ to CO over copper decorated g-C$_3$N$_4$ nanosheets with enhanced yield and selectivity, Appl. Surf. Sci. 427 (2018) 1165–1173.

[18] K. Wang, Q. Li, B. Liu, B. Cheng, W. Ho, J. Yu, Sulfur-doped g-C$_3$N$_4$ with enhanced photocatalytic CO$_2$-reduction performance, Appl. Catal. B 176 (2015) 44–52.

[19] J.-C. Wang, L. Zhang, W.-X. Fang, J. Ren, Y.-Y. Li, H.-C. Yao, J.-S. Wang, Z.-J. Li, Enhanced photoreduction CO$_2$ activity over direct Z-scheme α-Fe$_2$O$_3$/Cu$_2$O het-erostructures under visible light irradiation, ACS Appl. Mater. Interfaces 7 (2015) 8631–8639.

[20] Y. Zhang, A. Thomas, M. Antonietti, X. Wang, Activation of carbon nitride solids by protonation: morphology changes, enhanced ionic conductivity, and photo-conduction experiments, J. Am. Chem. Soc. 131 (2008) 50–51.

[21] J. Zhang, M. Zhang, L. Lin, X. Wang, Sol processing of conjugated carbon nitride powders for thin-film fabrication, Angew. Chem. Int. Ed. 127 (2015) 6395–6399.

[22] K. Xu, X. Li, P. Chen, D. Zhou, C. Wu, Y. Guo, L. Zhang, J. Zhao, X. Wu, Y. Xie, Hydrogen dangling bonds induce ferromagnetism in two-dimensional metal-free graphitic-C$_3$N$_4$ nanosheets, Chem. Sci. 6 (2015) 283–287.

[23] T.Y. Ma, Y. Tang, S. Dai, S.Z. Qiao, Proton-functionalized two-dimensional graphitic carbon nitride nanosheet: an excellent metal-/label-free biosensing platform, Small 10 (2014) 2382–2389.

[24] F. Cheng, H. Wang, X. Dong, The amphoteric properties of g-C$_3$N$_4$ nanosheets and fabrication of their relevant heterostructure photocatalysts by an electrostatic re-assembly route, Chem. Commun. 51 (2015) 7176–7179.

[25] D.J. Martin, K. Qiu, S.A. Shevlin, A.D. Handoko, X. Chen, Z. Guo, J. Tang, Highly efficient photocatalytic H$_2$ evolution from water using visible light and structure--controlled graphitic carbon nitride, Angew. Chem. Int. Ed. 53 (2014) 9240–9245.

[26] J. Lei, Y. Chen, L. Wang, Y. Liu, J. Zhang, Highly condensed g-C$_3$N$_4$-modified TiO$_2$ catalysts with enhanced photodegradation performance toward acid orange 7, J. Mater. Sci. 50 (2015) 3467–3476.

[27] H. Li, L. Zhou, L. Wang, Y. Liu, J. Lei, J. Zhang, In situ growth of TiO$_2$ nanocrystals on g-C$_3$N$_4$ for enhanced photocatalytic performance, Phys. Chem. Chem. Phys. 17 (2015) 17406–17412.

[28] Y. Bai, L. Ye, L. Wang, X. Shi, P. Wang, W. Bai, P.K. Wong, g-C$_3$N$_4$/Bi$_4$O$_5$I$_2$ het-erojunction with I3$^-$/I$^-$ redox mediator for enhanced photocatalytic CO$_2$ conver-sion, Appl. Catal., B 194 (2016) 98–104.

[29] T. Ohno, N. Murakami, T. Koyanagi, Y. Yang, Photocatalytic reduction of CO$_2$ over a hybrid photocatalyst composed of WO$_3$ and graphitic carbon nitride (g-C$_3$N$_4$) under visible light, J. CO$_2$ Util. 6 (2014) 17–25.

[30] Y. He, Y. Wang, L. Zhang, B. Teng, M. Fan, High-efficiency conversion of CO$_2$ to fuel over ZnO/g-C$_3$N$_4$ photocatalyst, Appl. Catal. B 168 (2015) 1–8.

[31] T. Di, B. Zhu, B. Cheng, J. Yu, J. Xu, A direct Z-scheme g-C$_3$N$_4$/SnS$_2$ photocatalyst with superior visible-light CO$_2$ reduction performance, J. Catal. 352 (2017) 532–541.

[32] M. Wang, M. Shen, L. Zhang, J. Tian, X. Jin, Y. Zhou, J. Shi, 2D-2D MnO$_2$/g-C$_3$N$_4$ heterojunction photocatalyst: in-situ synthesis and enhanced CO$_2$ reduction ac-tivity, Carbon 120 (2017) 23–31.

[33] N. Nie, L. Zhang, J. Fu, B. Cheng, J. Yu, Self-assembled hierarchical direct Z-scheme g-C$_3$N$_4$/ZnO microspheres with enhanced photocatalytic CO$_2$ reduction perfor-mance, Appl. Surf. Sci. 441 (2018) 12–22.

[34] S. Tonda, S. Kumar, M. Bhardwaj, P. Yadav, S. Ogale, g-C$_3$N$_4$/NiAl-LDH 2D/2D hybrid heterojunction for High-performance photocatalytic reduction of CO$_2$ into renewable fuels, ACS Appl. Mater. Interfaces 10 (2018) 2667–2678.

[35] A. Bafaqeer, M. Tahir, N.A.S. Amin, Synthesis of hierarchical ZnV$_2$O$_6$ nanosheets with enhanced activity and stability for visible light driven CO$_2$ reduction to solar fuels, Appl. Surf. Sci. 435 (2018) 953–962.

[36] I.A. Mkhalid, Preparation and characterization of NaBiO$_3$ nanopowders by different methods for photocatalytic reduction of CO$_2$, Ceram. Int. 40 (2014) 5795–5800.

[37] W. Jiang, X. Yin, F. Xin, Y. Bi, Y. Liu, X. Li, Preparation of CdIn$_2$S$_4$ microspheres and application for photocatalytic reduction of carbon dioxide, Appl. Surf. Sci. 288 (2014) 138–142.

[38] X. Jiao, Z. Chen, X. Li, Y. Sun, S. Gao, W. Yan, C. Wang, Q. Zhang, Y. Lin, Y. Luo, Defect-mediated electron–hole separation in one-unit-cell ZnIn$_2$S$_4$ layers for boosted solar-driven CO$_2$ reduction, J. Am. Oil Chem. Soc. 139 (2017) 7586–7594.

[39] H. Wang, L. Zhang, Z. Chen, J. Hu, S. Li, Z. Wang, J. Liu, X. Wang, Semiconductor heterojunction photocatalysts: design, construction, and photocatalytic perfor-mances, Chem. Soc. Rev. 43 (2014) 5234–5244.

[40] G. Yang, D. Chen, H. Ding, J. Feng, J.Z. Zhang, Y. Zhu, S. Hamid, D.W. Bahnemann, Well-designed 3D ZnIn$_2$S$_4$ nanosheets/TiO$_2$ nanobelts as direct Z-scheme photo-catalysts for CO$_2$ photoreduction into renewable hydrocarbon fuel with high effi-ciency, Appl. Catal. B 219 (2017) 611–618.

[41] M. Zubair, A. Razzaq, C.A. Grimes, S.-I. In, Cu$_2$ZnSnS$_4$ (CZTS)-ZnO: a noble metal-free hybrid Z-scheme photocatalyst for enhanced solar-spectrum photocatalytic conversion of CO$_2$ to CH$_4$, J. CO$_2$ Util. 20 (2017) 301–311.

[42] H. Zhao, X. Wang, J.-F. Feng, Y. Chen, X. Yang, S. Gao, R. Cao, Synthesis and characterization of Zn$_2$GeO$_4$/Mg-MOF-74 composites with enhanced photocatalytic activity for CO$_2$ reduction, Catal. Sci. Technol. (2018) 1288–1295.

[43] F.K. Butt, C. Cao, Q. Wan, P. Li, F. Idrees, M. Tahir, W.S. Khan, Z. Ali, M.J. Zapata, M. Safdar, Synthesis, evolution and hydrogen storage properties of ZnV$_2$O$_4$

glomerulus nano/microspheres: A prospective material for energy storage, Int. J. Hydrogen Energy 39 (2014) 7842–7851.

[44] F.K. Butt, C. Cao, R. Ahmed, W.S. Khan, T. Cao, N. Bidin, P. Li, Q. Wan, X. Qu, M. Tahir, Synthesis of novel ZnV_2O_4 spinel oxide nanosheets and their hydrogen storage properties, CrystEngComm 16 (2014) 894–899.

[45] F. Duan, W. Dong, D. Shi, M. Chen, Template-free synthesis of ZnV_2O_4 hollow spheres and their application for organic dye removal, Appl. Surf. Sci. 258 (2011) 189–195.

[46] A. Bafaqeer, M. Tahir, N.A.S. Amin, Synergistic effects of 2D/2D ZnV_2O_6/RGO nanosheets heterojunction for stable and high performance photo-induced CO_2 reduction to solar fuels, Chem. Eng. J. 334 (2018) 2142–2153.

[47] Z. Wang, J. Lv, J. Zhang, K. Dai, C. Liang, Facile synthesis of Z-scheme $BiVO_4$/ porous graphite carbon nitride heterojunction for enhanced visible-light-driven photocatalyst, Appl. Surf. Sci. 430 (2018) 595–602.

[48] M. Li, L. Zhang, X. Fan, M. Wu, M. Wang, R. Cheng, L. Zhang, H. Yao, J. Shi, Core-shell $LaPO_4$/g-C_3N_4 nanowires for highly active and selective CO_2 reduction, Appl. Catal. B 201 (2017) 629–635.

[49] H. Shi, G. Chen, C. Zhang, Z. Zou, Polymeric g-C_3N_4 coupled with $NaNbO_3$ nanowires toward enhanced photocatalytic reduction of CO_2 into renewable fuel, ACS Catal. 4 (2014) 3637–3643.

[50] Z. Wan, G. Zhang, X. Wu, S. Yin, Novel visible-light-driven Z-scheme $Bi_{12}GeO_{20}$/g-C_3N_4 photocatalyst: oxygen-induced pathway of organic pollutants degradation and proton assisted electron transfer mechanism of Cr (VI) reduction, Appl. Catal. B 207 (2017) 17–26.

[51] B. Tahir, M. Tahir, N.A.S. Amin, Photo-induced CO_2 reduction by CH_4/H_2O to fuels over Cu-modified g-C_3N_4 nanorods under simulated solar energy, Appl. Surf. Sci. 419 (2017) 875–885.

[52] M. Tahir, B. Tahir, N.A.S. Amin, Synergistic effect in plasmonic Au/Ag alloy NPs co-coated TiO_2 NWs toward visible-light enhanced CO_2 photoreduction to fuels, Appl. Catal. B 204 (2017) 548–560.

[53] Z. Yin, J. Qin, W. Wang, M. Cao, Rationally designed hollow precursor-derived $Zn_3V_2O_8$ nanocages as a high-performance anode material for lithium-ion batteries, Nano Energy 31 (2017) 367–376.

[54] T. Zhang, Y. Shen, Y. Qiu, Y. Liu, R. Xiong, J. Shi, J. Wei, Facial synthesis and photoreaction mechanism of $BiFeO_3$/$Bi_2Fe_4O_9$ heterojunction nanofibers, ACS Sustain. Chem. Eng. 5 (2017) 4630–4636.

[55] D. Ma, J. Wu, M. Gao, Y. Xin, T. Ma, Y. Sun, Fabrication of Z-scheme g-C_3N_4/RGO/ Bi_2WO_6 photocatalyst with enhanced visible-light photocatalytic activity, Chem. Eng. J. 290 (2016) 136–146.

[56] W.-J. Ong, L.-L. Tan, S.-P. Chai, S.-T. Yong, A.R. Mohamed, Surface charge modification via protonation of graphitic carbon nitride (g-C_3N_4) for electrostatic self-assembly construction of 2D/2D reduced graphene oxide (rGO)/g-C_3N_4 nanostructures toward enhanced photocatalytic reduction of carbon dioxide to methane, Nano Energy 13 (2015) 757–770.

[57] J. Bai, X. Li, G. Liu, Y. Qian, S. Xiong, Unusual formation of $ZnCo_2O_4$ 3D

[58] B. Xiao, H. Huang, X. Yu, J. Song, J. Qu, Facile synthesis of layered V_2O_5/ZnV_2O_6 heterostructures with enhanced sensing performance, Appl. Surf. Sci. 447 (2018) 569–575.

[59] Q. Xiang, J. Yu, M. Jaroniec, Preparation and enhanced visible-light photocatalytic H_2-production activity of graphene/C_3N_4 composites, J. Phys. Chem. C 115 (2011) 7355–7363.

[60] X. Lu, K. Xu, P. Chen, K. Jia, S. Liu, C. Wu, Facile one step method realizing scalable production of g-C_3N_4 nanosheets and study of their photocatalytic H 2 evolution activity, J. Mater. Chem. A 2 (2014) 18924–18928.

[61] Y. Hou, Z. Wen, S. Cui, X. Guo, J. Chen, Constructing 2D porous graphitic C_3N_4 nanosheets/nitrogen-doped graphene/layered MoS_2 ternary nanojunction with enhanced photoelectrochemical activity, Adv. Mater. 25 (2013) 6291–6297.

[62] M. Aslam, I.M. Ismail, T. Almeelbi, N. Salah, S. Chandrasekaran, A. Hameed, Enhanced photocatalytic activity of V_2O_5–ZnO composites for the mineralization of nitrophenols, Chemosphere 117 (2014) 115–123.

[63] J. Xu, W. Wang, S. Sun, L. Wang, Enhancing visible-light-induced photocatalytic activity by coupling with wide-band-gap semiconductor: a case study on Bi_2WO_6/ TiO_2, Appl. Catal. B 111 (2012) 126–132.

[64] S.-m. Chang, W.-s. Liu, Surface doping is more beneficial than bulk doping to the photocatalytic activity of vanadium-doped TiO_2, Appl. Catal. B 101 (2011) 333–342.

[65] M. Tahir, B. Tahir, N.A.S. Amin, Z.Y. Zakaria, Photo-induced reduction of CO_2 to CO with hydrogen over plasmonic Ag-NPs/TiO_2 NWs core/shell hetero-junction under UV and visible light, J. CO_2 Util. 18 (2017) 250–260.

[66] H. Liu, Z. Zhang, J. Meng, J. Zhang, Novel visible-light-driven $CdIn_2S_4$/mesoporous g-C_3N_4 hybrids for efficient photocatalytic reduction of CO_2 to methanol, J. Mol. Catal. 430 (2017) 9–19.

[67] L. Zhang, N. Li, H. Jiu, G. Qi, Y. Huang, ZnO-reduced graphene oxide nanocomposites as efficient photocatalysts for photocatalytic reduction of CO_2, Ceram. Int. 41 (2015) 6256–6262.

[68] X. Li, J. Chen, H. Li, J. Li, Y. Xu, Y. Liu, J. Zhou, Photoreduction of CO_2 to methanol over Bi_2S_3/CdS photocatalyst under visible light irradiation, J. Nat. Gas Chem. 20 (2011) 413–417.

[69] S. Zhang, X. Yin, Y. Zheng, Enhanced photocatalytic reduction of CO_2 to methanol by ZnO nanoparticles deposited on ZnSe nanosheet, Chem. Phys. Lett. 693 (2018) 170–175.

[70] T. Xiang, F. Xin, J. Chen, Y. Wang, X. Yin, X. Shao, Selective photocatalytic reduction of CO_2 to methanol in CuO-loaded $NaTaO_3$ nanocubes in isopropanol, Beilstein J. Nanotechnol. 7 (2016) 776–783.

[71] X. Li, H. Liu, D. Luo, J. Li, Y. Huang, H. Li, Y. Fang, Y. Xu, L. Zhu, Adsorption of CO_2 on heterostructure CdS (Bi_2S_3)/TiO_2 nanotube photocatalysts and their photocatalytic activities in the reduction of CO_2 to methanol under visible light irradiation, Chem. Eng. J. 180 (2012) 151–158.